Review

A synthesis of thermodynamic ablation at ice–ocean interfaces from theory, observations and models

Alena Malyarenko [a,b,*], Andrew J. Wells [c], Patricia J. Langhorne [a], Natalie J. Robinson [b], Michael J.M. Williams [b], Keith W. Nicholls [d]

[a] *Department of Physics, University of Otago, Dunedin, 9054, New Zealand*
[b] *National Institute of Water and Atmospheric Research, Wellington, 6022, New Zealand*
[c] *Atmospheric, Oceanic and Planetary Physics, Department of Physics, University of Oxford, Clarendon Laboratory, Parks Road, Oxford, OX1 3PU, UK*
[d] *British Antarctic Survey, High Cross, Madingley Road, Cambridge, CB3 0ET, UK*

ARTICLE INFO

ABSTRACT

Thermodynamic ablation of ice in contact with the ocean is an essential element of ice sheet and ocean interactions but is challenging to model and quantify. Building on earlier observations of sea ice ablation, a variety of recent theoretical, experimental and observational studies have considered ice ablation in contrasting geometries, from vertical to near-horizontal ice faces, and reveal different scaling behaviour for predicted ablation rates in different dynamical regimes. However, uncertainties remain about when the contrasting results should be applied, as existing model parameterisations do not capture all relevant regimes of ice–ocean ablation. To progress towards improved models of ice–ocean interaction, we synthesise current understanding into a classification of ablation types. We examine the effect of the classification on the parameterisation of turbulent fluxes from the ocean towards the ice, and identify the dominant processes next to ice interfaces of different orientation. Four ablation types are defined: melting and dissolving based on ocean temperatures, and shear-controlled and buoyancy-controlled regimes based on the dynamics of the near-ice molecular sublayer. We describe existing observational and modelling studies of sea ice, ice shelves, and glacier termini, as well as laboratory studies, to show how they fit into this classification. Two sets of observations from the Ross and Ronne Ice Shelf cavities suggest that both the buoyancy-controlled and shear-controlled regimes may be relevant under different oceanographic conditions. Overall, buoyancy-controlled dynamics are more likely when the molecular sublayer has lower Reynolds number, and shear for higher Reynolds number, although the observations suggest some variability about this trend.

Contents

* Corresponding author at: Department of Physics, University of Otago, Dunedin, 9054, New Zealand.
E-mail address: alena.malyarenko@niwa.co.nz (A. Malyarenko).

1. Introduction

The ocean drives the thermodynamic ablation of ice in a variety of geophysical settings: sea ice, ice shelves and glaciers. Basal ice ablation is a significant component of mass loss from the Antarctic Ice Sheet (Pritchard et al., 2012), contributing more than half of the total (Depoorter et al., 2013; Rignot et al., 2013; Liu et al., 2015). Increased glacial meltwater outflow from the Antarctic ice sheet has a range of effects: increase in large scale sea ice extent (Merino et al., 2018), local increase of sea ice thickness (Langhorne et al., 2015); reduction in bottom water formation (Silvano et al., 2018) and its freshening (Purkey and Johnson, 2013); positive feedback from reduced polynya activity leading to increased basal ablation of ice (Naughten et al., 2018a); global changes in the Southern Ocean (Timmermann and Hellmer, 2013) and impacts on the Meridional Overturning Circulation (Liu, 2018).

In the Northern Hemisphere, the reduction in Arctic sea ice observed over the last 4 decades is predicted to continue in the future (Meier, 2016; Notz and Bitz, 2016). The ablation of sea ice shows significant sensitivity to ocean heat flux (Maykut and Untersteiner, 1971) and is still challenging to predict on seasonal scales (Blanchard-Wrigglesworth et al., 2017). Meanwhile, ocean-linked recession of the calving faces of the Greenland glaciers has been observed over the last two decades (Rignot et al., 2010; Schaffer et al., 2017; Sciascia et al., 2013; Straneo et al., 2012; Straneo and Cenedese, 2015) but questions about submarine ablation still remain, as in situ observations are limited. Five Greenland glaciers have floating ice shelves today (Shroyer et al., 2017) and show similar uncertainties in ice sheet-ocean interaction to ice shelves surrounding Antarctica. Lack of understanding of Greenland and Antarctic Ice Sheet ablation is the largest source of uncertainty in the sea level rise predictions (Shepherd et al., 2012).

No unifying theory exists for all ocean-driven ablation of ice. In this study we use "ablation" to refer to thermodynamic ice loss into the ocean, driven by phase change; i.e. it is not caused by mechanical break off, such as iceberg calving. Ice ablation into the ocean takes place at the boundary next to sea ice, ice shelves, icebergs, glacier tongues and tidewater glaciers. Thermodynamic ablation depends on water and ice temperatures and composition, and velocity profiles. We do not discuss freezing in this work.

The ice–ocean thermodynamic balance is commonly described via a "3-equation" balance (e.g., Holland and Jenkins, 1999), where the salinity-dependent freezing temperature and the equations for the conservation of heat and salt are used to predict the interface salinity, temperature and ablation rate, given the far field temperature, salinity and water speed. While use of the balance formulation is presently widespread in ocean-coupled models, several terms are still not well constrained by observations. The coefficients used in the parameterisation of the transfer of heat, salt and momentum from the far field to the ice–ocean interface show the widest scatter. These parameterised fluxes

include implicit assumptions about mixing, stratification, the shape of density and velocity profiles, and the boundary layer thickness. If a study uses a parameterisation depending on the ocean velocity, the effects of basal friction also need to be explicitly taken into account. Differences in sea ice and ocean mixed layer conditions lead to a wide range of coefficient values when fitted to individual observations (e.g., Notz et al., 2003; Sirevaag, 2009; McPhee, 2016; Peterson et al., 2017). Using the same coefficient values for the vertical walls of tide-water glaciers, and the base of an ice shelf seems intuitively unrealistic. A lack of observations close to these interfaces introduces uncertainty in understanding the dominant physical processes and leads to large uncertainties in how key processes are modelled. Here we present an initial classification of ablation types, find similarities between all ice–ocean interfaces and point out the differences that require future research.

Ablation can be characterised via two thermal regimes: dissolving and melting, depending on the relative magnitudes of the ocean temperature and ice freezing temperature (e.g., Kerr, 1994a,b; Kerr and McConnochie, 2015; Notz et al., 2003; Wells and Worster, 2011; Woods, 1992). For example, a glacier terminating into water melts when the water is warm enough to bring the interface to the freezing temperature of pure water (i.e. 0 °C at surface pressure). Melting occurs both in fresh and salt water as long as the water is warm enough. However, there are many occasions where the phase change of ice occurs in contact with saline ocean water that is below the freezing temperature of pure freshwater (e.g., McPhee et al., 1987; Nicholls et al., 2012). For example, at 1000 m below sea level an ice shelf-ocean interface cannot melt if the surrounding ocean is below −0.75 °C (in-situ freezing point of fresh water). The phase change in this case is described as dissolving: a flux of salt from the ocean is directed towards the ice–ocean interface, lowering the local freezing point enough for a phase change to occur. During dissolution the ablation rate explicitly depends on the salt supply, which allows the local salinity-dependent freezing temperature at the interface to be significantly lower than the freezing temperature of ice. This process is described implicitly in large-scale ice–ocean models, although it is not always explicitly called dissolving.

Based on the water velocity, two turbulent flux regimes can be defined in the ocean boundary layer that affect ablation. They can be described as either buoyancy-controlled or shear-controlled (Wells and Worster, 2008). The thickness of the molecular sublayer adjacent to the interface is determined by different parameters in these regimes, and this influences how the heat flux through the ocean boundary layer should be parameterised. These physical mechanisms that drive mixing may be modulated by stratification in the boundary layer.

In this contribution we describe the essential characteristics of each regime and the transitions between regimes, based on existing laboratory, theoretical and modelling studies, and identify gaps in the field. We classify existing studies based on regime, and suggest that a wide range of published research, created for ice walls and

vertical plates, is applicable to an approximately horizontal ice shelf base. We also group sea ice and ice shelf studies by process, and note that some processes are not currently described in large-scale models. Accordingly, we will examine different approaches taken by ocean-focused and cryosphere-focused modelling. Finally, we compare existing ablation parameterisations to oceanographic observations from ice shelf cavities to understand ablation dynamics.

The paper is structured as follows: in Sections 2 and 3 we elaborate on the above described thermal and turbulent flux regimes, respectively. In Section 4, we provide classification criteria for ablation types and describe them for vertical, sloping and horizontal interfaces, noting possible effects of stratification and roughness on the ablation rate. In Section 5 we review existing modelling studies of ice–water ablation and, where possible, classify them by ablation type. We apply this ablation type classification to oceanographic observations from two ice shelf cavities in Section 6. Finally, in Section 7 we synthesise these strands and suggest several areas for future research.

2. Thermal regimes

In a system with a pure solid (e.g. an ice shelf) and a binary liquid (e.g. sea water) melting or dissolving allows the solid to lose mass by phase change (Woods, 1992; Kerr, 1994a,b; Notz et al., 2003; Wells and Worster, 2011). During melting, the phase change is driven by heat transfer from the liquid to the interface, while during dissolution the phase change happens in order to maintain chemical equilibrium at the interface. Woods (1992) developed the theory to include a binary solid and binary liquid, so the same ideas can be applied to a system of sea ice and sea water. Later, Hatton and Woods (2007) and Hatton and Woods (2008) demonstrated the dependence of dissolving on the composition of the ice, as different salts dissolve at different rates depending on the conditions. A practical application of dissolution has been studied by Wåhlin and Klein-Paste (2017), who investigated the dissolving of ice at −5 °C by different chemical solutions, with application to dissolving ice on roads.

During dissolution, salt is transferred to the interface where it depresses the local, salinity-dependent freezing temperature. The rate of salt transfer across the molecular sublayer can be two orders of magnitude smaller than that of heat transfer (McPhee et al., 1987; Steele et al., 1989), so salt transfer plays the limiting role on the rate of phase change. In contrast, during melting, the rate of phase change is unaffected by how quickly salt can be transferred, and is limited only by how fast the heat is transferred from the ocean to the interface. Asymptotic solutions show a transition region between melting and dissolving for cases of both diffusive transfer (Woods, 1992) and laminar convection (Wells and Worster, 2011). The decrease in far-field temperature required for a shift from melting to dissolving is not significantly different for diffusive and laminar transport (Wells and Worster, 2011). For laminar convection in the ocean next to an ice shelf, the transition from dissolving to melting occurs continuously over a range of temperatures between approximately −0.5 °C and +5.5 °C.

The difference between melting and dissolving can be clearly illustrated by temperature and salinity profiles in the boundary layer next to the interface (Fig. 1). This sketch is based on several works (e.g., Kerr, 1994a,b; Notz et al., 2003; Wells and Worster, 2011; Woods, 1992), but is illustrated here for a horizontal ice–water interface positioned above the saline water.

In the case of dissolving, both temperature and salinity profiles have non-zero gradients next to the interface. The salinity at the interface differs from the far-field salinity of the sea water and from the salinity of the ice. The interface is bound by a freezing point dependence, so the temperature there is below the freezing point of the ice in pure water. Ablation is driven by salt transfer from sea water to the interface and stops when the salinity profile has negligible gradient (i.e. there is no net salt transfer). Salt transfer is required to depress the salinity-dependent freezing temperature, hence dissolving is limited by salt
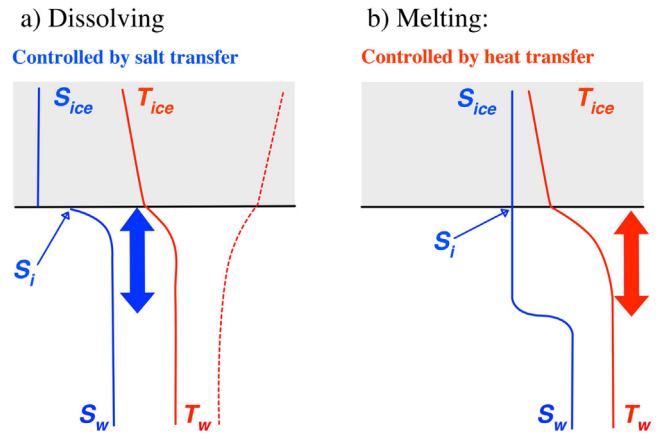

Fig. 1. Boundary layer profiles of temperature, T, (red) and salinity, S, (blue) in the two thermal regimes: dissolving and melting. During dissolving, salt transfer to the interface limits the phase change rate. During melting, a layer of meltwater is located next to the interface, and phase change is determined by the heat transfer. Two possible temperature profiles are plotted for dissolving: heat source for ablation coming from the ocean — solid line (e.g., Holland and Jenkins, 1999); heat source for ablation coming from the ice — dashed line (e.g., Notz et al., 2003). The gradients and layer thicknesses are not to scale. Blue arrow shows the salinity and temperature sublayer next to the interface. Where the salinity gradient is present, it limits the ablation rate. The red arrow shows the temperature sublayer, but no salinity gradient is present for melting, thus the ablation rate is not limited by salt transfer. Red and blue arrows show the immediate sublayer next to the interface, where either the salinity gradient is present/absent, thus limiting/not limiting the ablation rate. Subscripts i, ice, and w refer to ice interface, ice and water respectively.

transfer from the water to the interface. Woods (1992) showed that a warm solid can provide energy to allow phase change, demonstrating that the required heat does not have to be supplied by the liquid (dashed red profile in Fig. 1a).

In the case of melting (Fig. 1b), release of meltwater is sufficiently fast for a fresh water layer to develop immediately adjacent to the interface (Wells and Worster, 2011). The largest salinity gradients occur in an internal boundary layer slightly below the interface, and only the temperature profile has an appreciable gradient at the interface. In the layer adjacent to the interface salt transfer has no effect on the phase change rate and so melt rate is limited by heat transfer through this layer. Melting by this mechanism (rather than basal freezing) occurs as long as the heat supplied to the interface from the ocean exceeds that transferred from the interface through the ice shelf, which requires ocean temperatures to be significantly above the melting point of freshwater.

Large scale models that describe a thermodynamic balance between ice and ocean typically rely on the parameterisation of processes that happen in the ocean boundary layer adjacent to the interface. Conservation of heat and salt can be expressed by the Stefan condition and accompanying balance of solute fluxes across the ice–ocean interface. Additionally, the interface is described by the freezing point equation. Together this "3-equation balance" is the most common way to describe ablation, and can be formulated as follows:

$$-\rho_{ice}c_{ice}\gamma_T^{ice}(T_{ice} - T_i) + \rho_{ice}VL + \rho_w c_w \gamma_T \Delta T = 0, \tag{1}$$

$$-\rho_{ice}V(S_{ice} - S_i) + \rho_w \gamma_S \Delta S = 0, \tag{2}$$

$$T_i = aS_i + b + cp, \tag{3}$$

where $Q_T^{ice} = -\rho_{ice}c_{ice}\gamma_T^{ice}(T_{ice} - T_i)$ is the heat flux through the ice; $Q_T^{Latent} = \rho_{ice}VL$ is the latent heat flux from phase change; $Q_T^w = \rho_w c_w \gamma_T \Delta T$ is the heat flux through the water; $Q_S^{Brine} = \rho_{ice}V(S_{ice} - S_i)$ is the net salt flux from the ice–ocean interface resulting from ablation or freezing (where ablation results in negative Q_S^{Brine} and net freshening of the ocean), and $Q_S^w = \rho_w \gamma_S \Delta S$ is the salt flux through water. The

density of ice is ρ_{ice}, the density of water is ρ_w; c_{ice} is the specific heat capacity of ice, c_w is the specific heat capacity of water; L is the specific latent heat of fusion. The temperature, salinity and pressure at the interface are T_i, S_i, and p respectively, whilst a, b and c are empirical constants. The scalar transfer coefficients γ_T^{ice}, γ_T and γ_S have units of velocity, and control the flux resulting from change of the scalar ($\Delta T = T_i - T_w, \Delta S = S_i - S_w$) over the chosen distance. V is the rate at which the ice thins by ablation, positive for ablation, in m s^{-1} (e.g., Holland and Jenkins, 1999). Ablation of ice results in a volume flux of freshwater per unit area $\dot{w}$ satisfying $\rho_i \dot{w} = \rho_{ice} V$, where ρ_i is the density of the water at the ice–ocean interface. One can often approximate $\rho_i \sim \rho_w$ (accurate within a few percent). Please refer to Appendix A for nomenclature throughout this article, and to Appendix B for a summary of transfer coefficients. The role of γ_T^{ice} is to describe the heat flux within the ice shelf, representing advection of heat ($\gamma_T^{ice} = V$), or vertical diffusion of heat ($\gamma_T^{ice} = \kappa_{ice}/H$, where H is the thickness of the ice shelf, e.g., Holland and Jenkins, 1999). The role of the γ_T and γ_S parameterisation is to describe the ice–ocean fluxes of heat and salt in terms of the integral change of the parameter (temperature, salinity) between the interface and the ocean grid point position next to the ice, implicitly accounting for the unresolved turbulent dynamics. The choice of length scale determines the processes that transfer coefficients have to account for. In large-scale ocean models the melting and dissolving limits will emerge from Eqs. (1)–(3) and the flux parameterisations applied. However, it is important that these parameterisations adequately incorporate the fluid dynamic effects of the boundary layer structures.

To summarise, the thermal regime determines whether the ice is dissolving or melting, and impacts the structure of the ocean layer immediately adjacent to the ice ocean interface. The ice dissolves when large salt gradients and fluxes control the ablation rate, whilst the ice melts at warmer temperatures when the ablation rate is relatively independent of the flux of salt and is instead controlled by the heat flux.

3. Turbulent flux regimes

Our flow classification relies on the observation that turbulent production in the ice–ocean boundary layer will be controlled by either buoyancy forces or by shear. We initially review the turbulent flow regimes for thermal convection at a vertical surface. Later we argue these regimes may also apply under sufficiently steep slopes, and provide insights relevant to combinations of buoyancy and shear. Wells and Worster (2008) introduced a theory of convective regimes for thermally driven buoyant convection next to a heated wall that can be scaled up to geophysical scales. This has dynamical similarities with buoyancy-driven convection of fresh water released at an ice face. We do not expect to see laminar convection over any appreciable scale in the geophysical situation, but we are interested in the two turbulent flux regimes: buoyancy-driven and shear-driven. Wells and Worster (2008) envisaged the buoyancy force as a mechanism to generate turbulence and flow along the interface. It thus needs an ice shelf with an appreciable basal slope, and cannot occur for flow under horizontal ice faces. The buoyancy force also provides the stabilising effect of stratification for non-vertical faces, although this is not a direct agent for turbulent production. For flow below horizontal ice faces, the turbulent fluxes would either be controlled by the shear regime due to external flows (possibly modified by stable stratification), or double-diffusive turbulence in quiescent settings (discussed in more detail in Sections 4.3, 4.4). We thus use the terms buoyancy-controlled flux regime, which includes both direct buoyancy-driven convection as described in Wells and Worster (2008) and double-diffusive turbulence (c.f. Keitzl et al., 2016a), and shear-controlled flux regime throughout this article to highlight differences in the two flux parameterisations. Fig. 2 shows the transition from laminar convection to buoyancy-controlled turbulent convection and then shear-controlled turbulent convection, and the corresponding impact on the molecular sublayer. It is important to note that the differing effects of the buoyancy force on the production of turbulence via along slope flow, and the suppression
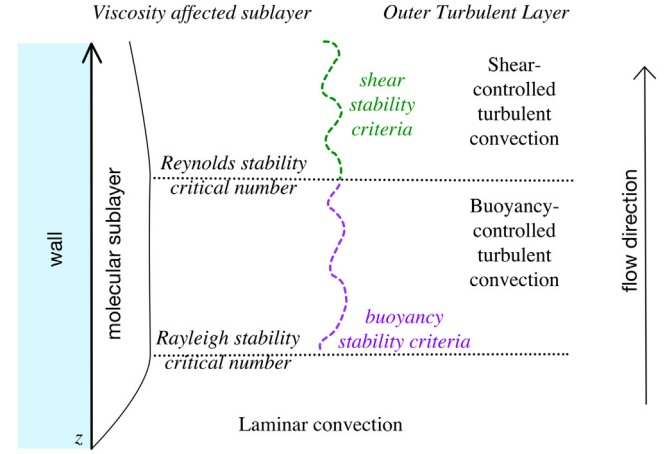
Fig. 2. Turbulent flux regime hierarchy next to a vertical wall: laminar convection, buoyancy-controlled turbulent convection, and shear-controlled turbulent convection. A sublayer with thickness δ exists next to the interface, where molecular transport dominates. Next, a sublayer affected by viscosity and the outer layer (fully turbulent) are defined. At intermediate heights, the width of the molecular sublayer is defined by the buoyancy stability criterion (Eq. (4)). At large heights, the width of the molecular sublayer is consistent with shear stability criterion (Eq. (5)). This is a simplified version of Figs. 1 and 2 in Wells and Worster (2008).

of turbulent mixing via vertical stratification will vary for interfaces with different orientations.

A boundary layer exists in the ocean next to an ice–ocean interface. Inside the boundary layer, we can define a molecular sublayer, where molecular transport dominates, and the outer turbulent layer, dominated by inertia and turbulent transport (e.g. Wells and Worster, 2008). By contrast, for flow under ice shelves with shallow slope, the region of turbulent transport is likely to be dominated by Coriolis forces, and might be subject to a balance of Coriolis and buoyancy forces (c.f. Jenkins, 2016). The following discussion is based on single component convection along a vertical wall, while slopes are considered later. The difference between heat flux expressions for the different turbulent-flux regimes is determined by how the thickness of the molecular sublayer is calculated. For vertical boundaries, the system is described using dimensionless numbers:

$$Ra_\delta = \frac{g' \delta^3}{\kappa \nu}, \tag{4}$$

$$Re_\delta = \frac{W \delta}{\nu}, \tag{5}$$

where a condition $Ra_\delta = constant$ represents a buoyancy stability criterion, and a condition $Re_\delta = constant$ is a shear stability criterion. Here, δ is the molecular sublayer thickness, W is the mean vertical velocity of the boundary layer, ν is kinematic viscosity, κ is thermal diffusivity, and $g' = \frac{g(\rho_\infty - \rho_i)}{\rho_\infty}$ is the reduced gravity based on the density difference between the far field (ρ_∞) and interfaces values.

For the regime with buoyancy-controlled fluxes, the molecular sublayer thickness is determined by a constant Ra_δ (Eq. (4), see Wells and Worster, 2008). In this case, the molecular sublayer thickness is intrinsically determined, and it depends on the density difference between the interface and the ambient layers. As velocities outside of the molecular sublayer grow and the boundary layer Reynolds number Re_δ attains a critical value Re_c for shear instability, the outside layer begins to exert shear on the molecular sublayer and the thickness of the molecular sublayer is instead determined by a constant Re_δ (Eq. (5), see Wells and Worster, 2008). In this case, the thickness of the molecular sublayer is determined by the mean water velocity W. Thus the switch between the turbulent flux regimes depends on the strength of flow in the turbulent outer layer, with the thickness of the molecular sublayer changing between regimes. The current observational evidence does not fully constrain a specific threshold value Re_c for shear instability,

which could in principle depend on the specific velocity variation with distance from the ice face. Wells and Worster (2008) gave an approximate estimate by drawing analogy with shear instability of a Blasius boundary layer flow. The resulting transitions between regimes are defined in Fig. 3.

The changing molecular sublayer thicknesses yield expressions for heat and salt flux formulations consistent with studies of an ice–water interface from the literature (Fig. 3). A scaling estimate for the heat flux through the boundary layer h yields $q = \rho_w c_w \kappa \left.\frac{\partial T}{\partial z}\right|_{z=h} \sim \rho_w c_w \kappa \frac{\Delta T}{\delta}$. In that case, δ is estimated differently in the two turbulent flux regimes. First from Eq. (4), in the buoyancy-controlled regime $\frac{1}{\delta} = \left(\frac{g'}{\kappa \nu Ra_\delta}\right)^{1/3}$, so $q \sim \rho_w c_w \left(\frac{g' \kappa^2}{\nu Ra_\delta}\right)^{1/3} \Delta T$. Analogously, for compositional convection, Kerr and McConnochie (2015) define the salt flux as $F_S = \frac{D \Delta S}{h_c} \sim \gamma \left(\frac{g' D^2}{\nu}\right)^{1/3} \Delta S$, where the constant $\gamma \sim \left(\frac{1}{Ra_\delta}\right)^{1/3}$. In constructing these scaling estimates, we have assumed that the temperature and salinity drops across the molecular sublayer are a similar order of magnitude to the total temperature and salinity differences across the boundary layer. Second in a shear-controlled regime from Eq. (5), $\frac{1}{\delta} = \frac{W}{\nu Re_\delta}$, so $q \sim \rho_w c_w W \frac{\kappa}{\nu Re_\delta} \Delta T$. This case is analogous to the widely used parameterisation of heat flux first defined in (McPhee et al., 1987) with $Q_T = \rho_w c_w u_* \Gamma_T \Delta T = \rho_w c_w U \left(C_d^{1/2} \Gamma_T\right) \Delta T$. Assuming that the velocity at the edge of the sublayer is of similar order of magnitude to the mean velocity in the boundary layer, the scaling argument of Wells and Worster (2008) based on the shear instability criterion for the molecular sublayer yields $C_d^{1/2} \Gamma_T \sim \frac{\kappa}{\nu Re_\delta}$ (Fig. 3). For a pure stratified shear flow at a horizontal boundary, McPhee et al. (1987) derive a more complex expression for the prefactor $C_d^{1/2} \Gamma_T$ that more fully accounts for velocity variation over the log layer and the impact of stratification, although current observations are insufficient to distinguish this from a constant coefficient (see discussion in Jenkins, 2011).

The way the thickness is determined suggests that the heat flux shows dependence on different parameters in the buoyancy-controlled and shear-controlled flux regimes. In the buoyancy-controlled regime for thermal convection, the heat flux through the entire boundary layer depends primarily on the temperature difference (i.e. density difference) between the interface and the turbulent layer. In contrast, in the shear-controlled regime for thermal convection, the heat flux through the entire boundary layer depends on the same temperature difference (i.e. density difference) and the characteristic velocity of the outer turbulent layer (as velocity determines δ through Re_δ). The different scalings for heat and salt fluxes give quite different predictions for the ablation rates, thus using the appropriate scaling is essential.

For both convective flow from a melting ice face, and heat transfer from a heated vertical surface (Wells and Worster, 2008), local dimensionless numbers can be defined as a function of height as shown in Fig. 3. The heat flux through the boundary layer, q, can be characterised by the local Nusselt number $Nu_z = \frac{qz}{\rho_w c_p \kappa \Delta T}$ expressed in terms of the local Rayleigh number $Ra_z = \frac{g' z^3}{\kappa \nu}$, where z is distance from the leading edge of the ice face where flow is initiated (i.e., base of the terminus for the glacier termini, or the grounding line for ice shelves). The relationship between these numbers provides an expression for the heat flux across the boundary layer through the thickness of the molecular sublayer.

To summarise, the type of turbulent flux regime determines the thickness of the molecular sublayer and how this thickness is calculated.

4. Ablation types

For ice ablation, both heat and salt transport are relevant, with release of fresh meltwater providing a buoyancy source. The turbulent flux and the thermal regimes both affect the ablation rate due to the boundary layer structure. This informs the basis for the classification of ablation types, first described for a vertical interface by Wells (2008). The underlying assumptions used are: (1) during melting, a freshwater layer is located next to the interface (with salinity nearly equal to the

salinity of the solid); (2) during dissolving, the salinity at the interface differs significantly from both the salinity of the ice and the salinity of the ambient water; and (3) the shear-controlled regimes have a well-mixed outer boundary layer that likely extends further from the interface than the buoyancy-controlled regime.

Transitions between dissolving and melting have been considered for diffusive transport (Woods, 1992), in the presence of laminar compositional convection (Wells and Worster, 2011) and for horizontal surfaces where buoyant melt convects through the overriding fluid, located above the interface (Kerr, 1994a,b). Below we review theoretical and experimental studies relevant to these transitions occurring for melting glacier termini, ice shelves and sea ice, for cases where a turbulent and buoyant flow is confined from the side or from above. The turbulent melting regime has been the least studied, and theories for the transition between turbulent dissolving and melting have not yet been tested against observations. The existing solutions are highly dependent on the orientation of the ice–water boundary. As a result, next we describe how interface orientation affects the results. We provide a reference tree of the studies that suggested new ablation parameterisations and show the theory development in Fig. 4. Modelling studies will be described in Section 5.

4.1. Vertical interface

A plume of meltwater rising along a vertical ablating interface sustains convection. In laminar convection next to a wall Wells and Worster (2011) showed asymptotic solutions for melting and dissolving. The difference between melting rates and dissolving rates depends not only on thermal and salt diffusivities, but also on the boundary layer thickness and changing interfacial salinity. Thus there is a smooth transition between slow dissolution rates and slightly faster melting rates. As the rising plume transforms from laminar to buoyancy-controlled to shear-controlled, increased mixing can lead to a larger difference between melting and dissolving solutions (Wells, 2008).

Pioneering work on ice ablation was done in the 1980s (Huppert, 1989; Huppert et al., 1984; Huppert and Josberger, 1980; Huppert and Sparks, 1988; Huppert and Turner, 1980, 1981; Josberger and Martin, 1981). For wall ablation, bidirectional flow next to the interface has been described for the laminar sublayers (Josberger and Martin, 1981). In the case of a stratified liquid, the spread of meltwater in horizontal layers has been observed (Huppert and Turner, 1980, 1981; Jacobs et al., 1981).

Laboratory experiments and Direct Numerical Simulations (DNS) experiments have studied the ablation of a vertical ice–water interface in a variety of conditions, and have been compared with results from a theory developed to quantify fluxes at a horizontal interface (Kerr, 1994a,b). First, Kerr and McConnochie (2015) and Gayen et al. (2016b) considered an ice wall adjacent to water of constant salinity and made a series of experiments with water temperatures between 0 and 6 °C. In this case, the ablation was characterised as buoyancy-controlled dissolving, with the observed ablation rate consistent with $\dot{w} = const \times (T_w - T_L(S_w))^{1.34}$, thus confirming the independence of ablation from the mean plume velocity during buoyancy-controlled dissolving. The power 4/3 arises from $(\rho_w - \rho_i)^{\frac{1}{3}} (S_w - S_i)$ (Kerr and McConnochie (2015), Eq. (2.23)), where both density and salinity differences show linear dependency on $(T_w - T_L(S_w))$. The authors note that when the water temperature exceeds 3–4 °C above the freezing point, a transition into turbulent melting is approached (rather than dissolving) and estimated that the interface temperature is overestimated by their analysis. Complimentary DNS modelling (Gayen et al., 2016b) confirms the same power-law dependence of dissolving rate on temperature difference as in the laboratory observations.

The transition between buoyancy-controlled and shear-controlled regimes next to a wall has been discussed by Kerr and McConnochie (2015). The transition is predicted to happen at $Ra_z = 10^{16}$ for the thermal convection of air (based on the Prandtl number, Grossmann and Lohse, 2000). However, for compositional convection during ice ablation the transition between turbulent flux regimes occurs at
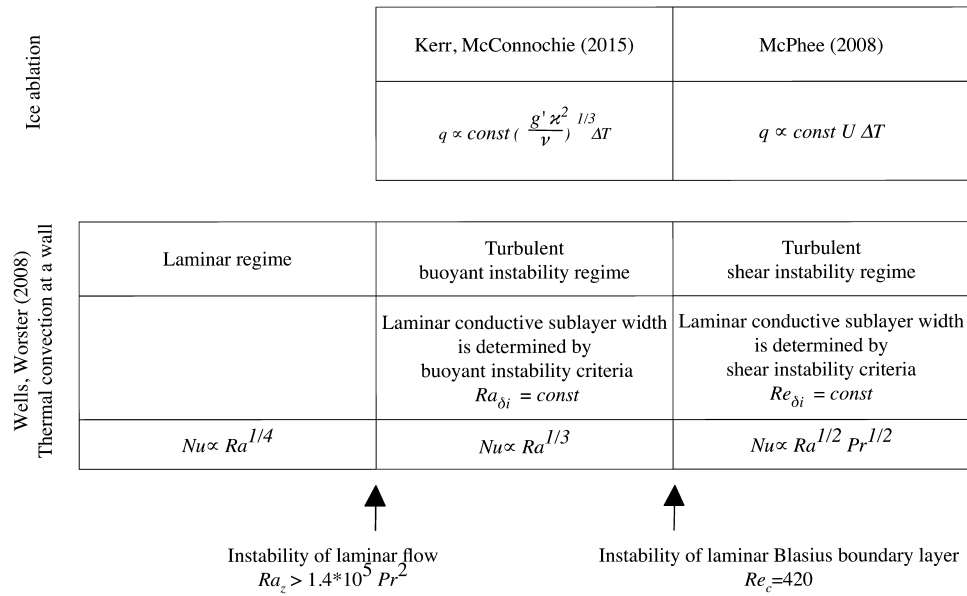
	Kerr, McConnochie (2015)	McPhee (2008)
	$q \propto const \left(\frac{g' \varkappa^2}{\nu} \right)^{1/3} \Delta T$	$q \propto const \, U \, \Delta T$

Laminar regime	Turbulent buoyant instability regime	Turbulent shear instability regime
	Laminar conductive sublayer width is determined by buoyant instability criteria $Ra_{\delta i} = const$	Laminar conductive sublayer width is determined by shear instability criteria $Re_{\delta i} = const$
$Nu \propto Ra^{1/4}$	$Nu \propto Ra^{1/3}$	$Nu \propto Ra^{1/2} \, Pr^{1/2}$

Ice ablation (left margin, top section)

Wells, Worster (2008) Thermal convection at a wall (left margin, bottom section)

Instability of laminar flow
$Ra_z > 1.4 \ast 10^5 \, Pr^2$

Instability of laminar Blasius boundary layer
$Re_c = 420$

Fig. 3. Turbulent flux regimes and resulting heat and salt flux parameterisations from different studies. Bottom row: classification of Wells and Worster (2008) for thermal convection next to a wall. Top row: Similarities of heat flux definitions in existing ice–ocean research.

$Ra_z = 10^{21}$ (based on the Schmidt number, see Kerr and McConnochie, 2015). McConnochie and Kerr (2017) considered experiments for a vertical ice wall where the flow velocity is enhanced by the introduction of a significant buoyancy source, simulating effects of subglacial discharge. They found that the transition between buoyancy and shear regimes occurs at a plume speed of 0.03–0.05 m s^{-1} for water at +3.5 °C.

Such small-scale studies provide a unique ability to examine interface conditions and boundary layer development in a controlled environment, that cannot be obtained in field observations. In general, however, such small-scale studies do not reach Rayleigh numbers that are typically observed next to an ice–ocean interface in the field, and scaling of the results is not a trivial task.

In reality many glaciers are confined in fjords in complex geometries. Recently, a series of laboratory studies were conducted in order to understand glacier ablation on a fjord scale. Sciascia et al. (2014) and Cenedese and Gatto (2016a) showed in laboratory experiments that the ablation rate of a glacier terminus directly depends on the fjord dynamics and subglacial discharge (which impacts water velocity and temperature). Cenedese and Gatto (2016b) tested the impact of discharge source locations: two closely located discharge sources acting as one large plume cause more melting than if they are located far apart, even though the area of melting is smaller.

The grounding line region of Antarctic glaciers remain underobserved, with a handful of studies providing in situ ocean forcing (e.g., Sugiyama et al., 2014). Tidewater glaciers have been a subject of observational studies recently, providing insight into ocean conditions in the fjords of Greenland (reviewed by Straneo and Candedese, 2015; see also Cape et al., 2019; Carroll et al., 2018; Jackson and Straneo, 2016; Mankoff et al., 2016; Moon et al., 2018; Schild et al., 2018; Slater et al., 2018; Straneo et al., 2010, 2012), Alaska (Motyka et al., 2003) and Patagonia, where a glacier is in direct contact with waters of 8–11 °C (Moffat et al., 2018). Similarly, icebergs may float into warm Atlantic waters (Yankovsky and Yashayaev, 2014). All of these ice interfaces are subject to melting. Nonetheless, the "wall" ablation of glacier termini is tricky to measure.

4.2. Sloping interface

Incorporating the effect of the interface slope can be done directly in the thermodynamic balance, or through modification of the ocean velocity calculation when in the shear regime. For Ice Shelf Water plumes (Jenkins, 1991; Jenkins and Bombosch, 1995, and derivatives

thereof) the effects of basal slope are included in the buoyancy force that drives the flow and in the entrainment calculation. For a gentle slope (slopes of 10^{-2} and less) the buoyancy of the plume is balanced by friction.

Wells (2008) calculated transitions under a sloping interface for a plume model of natural convection under an ice shelf base. In this case W is interpreted as the alongslope velocity, and δ and $(\rho_\infty - \rho_i)$ are measured normal to the interface. For steep slopes with $\tan \varphi \gg 0.014$ (where $\varphi = 0$ is horizontal), the theory suggests that the boundary layer model (described here in Section 3) can be safely applied to thermal convection, with the reduced gravity normalised by the slope, $g' = g(\rho_\infty - \rho_i) \sin \varphi / \rho_\infty$. The distance from the leading edge to the transition to turbulent flow increases for more shallow angles, due to the weaker alongslope component of the buoyancy force. But the distance between the initial buoyancy instability and the subsequent shear instability decreases for more shallow angles (i.e. the shear-controlled regime arrives more readily). From Eq. (4) we can see that to maintain the buoyancy stability criterion with smaller g', a larger δ is required. The larger δ then allows the shear instability criterion Eq. (5) to be attained with smaller alongslope velocity W than is necessary for steeper slopes. For convection dominated by differences in salinity, Wells (2008) argued that this boundary layer model applies for slopes with angle $\tan \varphi \gg 0.001$. Assuming that the boundary layer model is valid for a slope $\tan \varphi = 0.002$ as used in Jenkins (1991) and Wells (2008) estimated that the surface would be in the shear-controlled regime when the distance along the slope is >900 m. However, these transition angles have not been tested in the field or in laboratory experiments, and so the results should be treated with appropriate caution.

For sloping ice faces in the buoyancy-controlled regime, the solution for the thermodynamic balance of a vertical wall is modified by accounting for the angle of the interface. McConnochie and Kerr (2018) and Mondal et al. (2019) showed that the ablation rate scales as $(\sin \varphi)^{2/3}$ times the vertical wall case. This approach relies on the buoyancy-driven flow of meltwater along the interface. As a result, under a horizontal interface such a parameterisation produces no ablation at all. McConnochie and Kerr (2018) recommend applying their parameterisation to slopes of more than 2° to the horizontal.

The above scalings and arguments do not account for the influence of Coriolis forces. Jenkins (2016) considered the boundary layer dynamics with Coriolis forces assuming a constant eddy viscosity, and
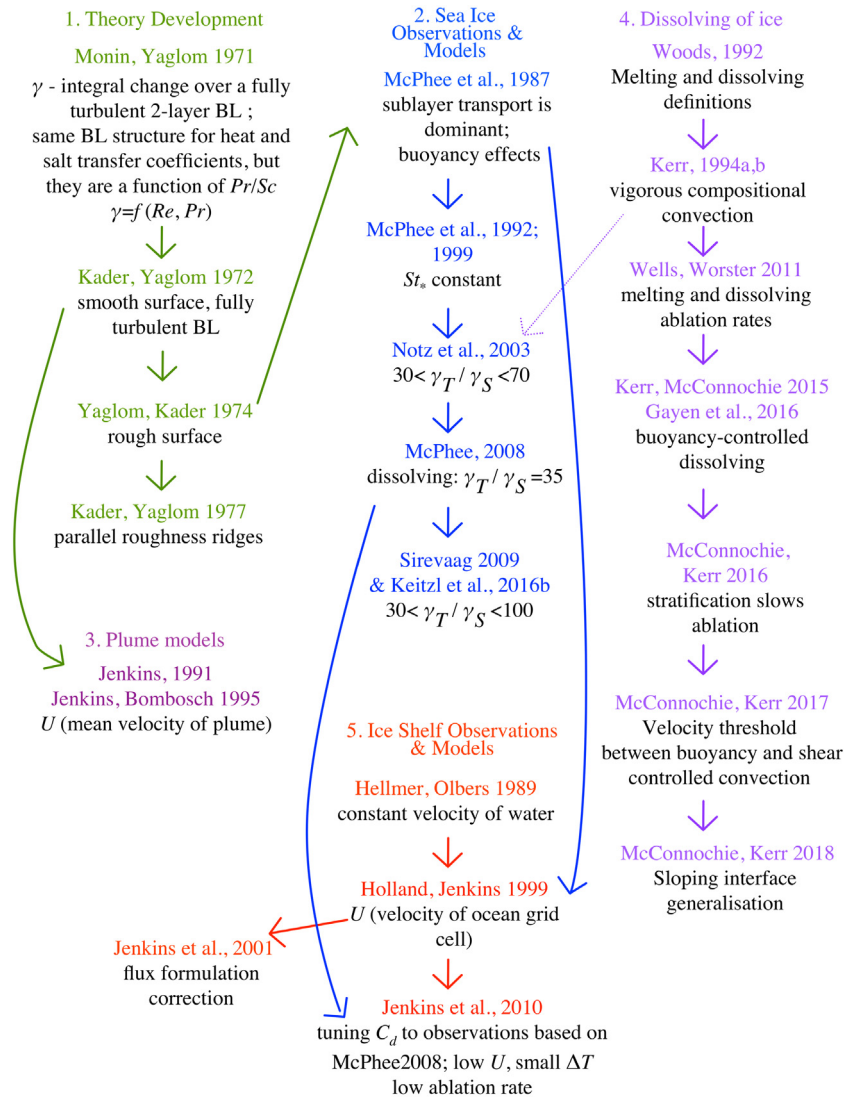
1. Theory Development

Monin, Yaglom 1971
γ - integral change over a fully turbulent 2-layer BL ; same BL structure for heat and salt transfer coefficients, but they are a function of Pr/Sc
$\gamma = f(Re, Pr)$

Kader, Yaglom 1972
smooth surface, fully turbulent BL

Yaglom, Kader 1974
rough surface

Kader, Yaglom 1977
parallel roughness ridges

3. Plume models

Jenkins, 1991
Jenkins, Bombosch 1995
U (mean velocity of plume)

2. Sea Ice Observations & Models

McPhee et al., 1987
sublayer transport is dominant; buoyancy effects

McPhee et al., 1992; 1999
St_* constant

Notz et al., 2003
$30 < \gamma_T / \gamma_S < 70$

McPhee, 2008
dissolving: $\gamma_T / \gamma_S = 35$

Sirevaag 2009
& Keitzl et al., 2016b
$30 < \gamma_T / \gamma_S < 100$

5. Ice Shelf Observations & Models

Hellmer, Olbers 1989
constant velocity of water

Holland, Jenkins 1999
U (velocity of ocean grid cell)

Jenkins et al., 2001
flux formulation correction

Jenkins et al., 2010
tuning C_d to observations based on McPhee2008; low U, small ΔT low ablation rate

4. Dissolving of ice

Woods, 1992
Melting and dissolving definitions

Kerr, 1994a,b
vigorous compositional convection

Wells, Worster 2011
melting and dissolving ablation rates

Kerr, McConnochie 2015
Gayen et al., 2016
buoyancy-controlled dissolving

McConnochie, Kerr 2016
stratification slows ablation

McConnochie, Kerr 2017
Velocity threshold between buoyancy and shear controlled convection

McConnochie, Kerr 2018
Sloping interface generalisation

Fig. 4. Development of the ablation parameterisations used in a range of existing studies: a consecutive reference tree, which supports classifications of studies based on assumptions made in the "parent" research. Studies are grouped by topics: 1. Theory Development (green), 2. Sea Ice Observations and Models (blue), 3. Plume Models (plum), 4. Dissolving of ice (purple), 5. Ice Shelf Observations & Models (red). Significant influence of research within and across groups is signified by arrows. A short description of papers, relevant to this review, is added in black.

neglecting alongslope gradients in temperature and salinity along with flow inertia. For buoyancy-driven upslope flows this predicts a nested boundary layer structure, with an outer region of the boundary layer featuring the balance of Coriolis and buoyancy forces, transitioning to an inner Ekman layer close to the ice face where viscous forces become important. The solutions of Jenkins (2016) rely on assumed eddy diffusivities to parameterise eddy fluxes of heat, salt and momentum. Hence it remains an open question as to how to reconcile this approach with scalings for turbulent heat and salt fluxes into the molecular sublayer.

More steeply sloping ice–water interfaces can be found in ice shelf crevasses and ice shelf frontal regions. External velocity sources, such as tidal currents, can significantly complicate the entrainment rate and the boundary layer structure next to the sloping interface. Another complication for parameterising melt arises through the horizontal resolution of models. Neither an ice shelf base, nor the lower boundary of sea ice, are not perfectly smooth, and the ablation rate varies nonlinearly with the base angle. Thus, using a parameterisation based on the slope averaged over a model grid cell will not necessarily match the average value of the locally determined ablation rate. Accurately capturing the slope dependence, potentially with eddy-resolving models, is important because variable ablation under ice shelves can lead to the formation

of basal channels, where the slope of the interface changes in space and time (e.g. Alley et al., 2016; Dallaston et al., 2015; Gladish et al., 2012; Sergienko et al., 2013). In particular, linear stability analysis suggests that the emergent lengthscales of such basal channels can sometimes depend sensitively on the magnitude of turbulent diffusive mixing (Dallaston et al., 2015), and so it may be important to accurately characterise eddy-induced mixing.

4.2.1. Ice shelf-ocean observations

For the ice shelf case, potential sources of shear-controlled flow include buoyancy driving in the boundary layer, tides (including any flow induced by tidal flexure of the ice shelf in grounding zones), and background geostrophic currents forced by large scale pressure gradients. In contrast to sea ice, the atmospheric wind stress does not substantially move the base of an ice shelf relative to the water below — and hence momentum flux beneath ice shelves is not a source of shear. The roughness of an ice shelf base is not yet well known but could be a factor in the shear distribution in the boundary layer. Warm intrusions of surface water (Mode 3 circulation, Hattermann et al., 2012; Malyarenko et al., 2019) and deep waters (Mode 2 circulation, Hellmer et al., 2012) could move ice from dissolving to melting regimes

with increased ocean warming. Direct observation of the ice shelf-ocean interface is extremely difficult to achieve and thus rare. Currently the largest set of observations has been collected for the Filchner–Ronne Ice Shelf, a selection of which are described in Jenkins et al. (2010b); Nicholls et al. (1997), Nicholls et al. (2004) and Nicholls et al. (2009). Limited observations are available for Larsen C (Nicholls et al., 2012; Davis and Nicholls, 2019), Ross (Arzeno et al., 2014; Jacobs et al., 1979; Stern et al., 2013; Stewart et al., 2019), McMurdo (Robinson et al., 2010, 2014), George VI (Kimura et al., 2015; Potter and Paren, 1985), Fimbul (Hattermann et al., 2012), Sørsdal (Gwyther et al., 2020), Pine Island (Davis et al., 2018; Jenkins et al., 2010a; Kimura et al., 2016; Stanton et al., 2013), and Amery (AMISOR Project, 6 moorings over 2001–2012, Craven et al., 2014; Herraiz-Borreguero et al., 2013, 2015) Ice Shelves.

A small subset of these (Jenkins et al., 2010b; Kimura et al., 2015; Stewart et al., 2019; Stanton et al., 2013) have simultaneous observations of the three ocean variables (temperature, salinity and velocity) that are required to determine ablation rate, as well as the direct measurement of ablation rate. In these cases, oceanographic instruments have necessarily been located away from the interface and often only represent point measurements, thus limiting our understanding of boundary layer structure. Snapshots of boundary layer structure are available from CTD profiles, but stations with continuous profiling show that the structure can change rapidly and assumptions of stratification cannot be extrapolated with confidence in time or space. Despite these limitations, Jenkins et al. (2010b) represent a study in which ice shelf cavity observations have been used to test the ice–ocean flux parameterisations, with good agreement with the parameterisation for the shear-controlled regime in conditions of significant tidal flow. We are unaware of any field tests relevant to the buoyancy-controlled regime under sloping shelves, although Kimura et al. (2015) observed double diffusive staircases below very shallow slopes (see below).

The set of useful observations is constrained for a variety of reasons. Vertically continuous observations of temperature, such as fibre-optic measurements and thermistor cables (Jenkins et al., 2010b; Stern et al., 2013), provide a first order approximation of the boundary layer structure and ablation rates (Kobs et al., 2014). However, as salinity is the factor that is dominant in determining density in cold water, we need to measure salinity at similar resolution, or else rely on knowing the temperature–salinity relationship (e.g., Gade, 1979). Data are also available from autonomous underwater vehicles (Jenkins et al., 2010a; Kimura et al., 2016; Nelson et al., 2017; Nicholls et al., 2006; Gwyther et al., 2020), but observations were not always supported with simultaneous melt rates and they are not available as long time series.

Direct observations of the basal ablation rate of ice shelves have been gathered with upward looking altimeters through boreholes (Stanton et al., 2013; Stewart et al., 2019) or phase-sensitive radars (Begeman et al., 2018; Jenkins et al., 2010a; Nicholls et al., 2015; Gwyther et al., 2020). Remote observation of basal ablation, such as satellite observations, provide estimates that are heavily spatially filtered, and are often unreliable near grounding lines, where they calculate basal ablation as a residual of various processes that are often poorly constrained (Mouginot et al., 2014). The results provide a good indication of patterns of basal mass balance, but do not yet provide detailed time series

4.3. Horizontal interface

The theories for pure compositional (salinity-driven buoyant) convection break down for the case with an approximately horizontal ice–ocean interface i.e. the "roof case", which is the geometry most closely representing an ice shelf base and the bottom boundary of sea ice. In the case of a horizontal roof, the release of fresh meltwater creates a stably stratified layer next to the interface, with no alongslope component of the buoyancy force to drive flow. We expect the ablation rate to depend on the erosion of this stably stratified layer

by external shear flows, or in quiescent environments, the ablation rate could be controlled by double diffusive turbulence (e.g., Kimura et al., 2015). Stable stratification next to the ice interface may also reduce mixing in the boundary layer, in regimes where the heat transfer across the molecular sublayer is driven by shear-controlled turbulence. For horizontal surfaces, we apply the term "buoyancy-controlled" flux regime to describe double-diffusive turbulence generated by destabilising buoyancy forces. We however note that the "shear-controlled" regime where turbulence is produced by shear, may also be influenced by stabilising buoyancy forces in highly stratified conditions created by buoyant meltwater release.

Combining laboratory experiments and DNS, Keitzl (2015), Keitzl et al. (2016a,b) studied a horizontal ice–water interface in experiments with water temperatures from 2.9 to 47.9 °C. In this work ice was located on top of a water tank, so the setup simulates ice shelf and sea ice conditions. Experiments in a fresh water–fresh ice system (Keitzl et al., 2016a) are influenced by nonlinearity of the equation of state with no salinity effects. This system showed that stable stratification in the water column close to the ice–water interface shielded the interface and diminished the melt rate. In a purely convection-driven case, Keitzl (2015) observed that convective motions were not strong enough to overcome the diffusive shield. In the system with stable salt stratification Keitzl et al. (2016b), found that meltwater production increased the stratification, which increased shielding and diminished the melt rate in all experiments. Both freshwater and sea water experiments showed that the melt rate can be described as a function of the convective Richardson number, defined as a ratio of relative strength of interface shielding to convective velocity scale: $\dot{w} \sim Ri_*^n$, where $n = -0.75$ for sea water and $n = -0.40$ for fresh water system (in the sea water system the influence of convective velocity on the melt rate is stronger). We can infer that in realistic ice–ocean conditions, a stably stratified diffusive layer is expected to shield the interface from the turbulent outer layer until the turbulence is so strong that the diffusive layer diminishes and no longer has the controlling effect. However, regime classification, as described in Sections 2 and 3, has not been applied in these studies.

An insight into the shear-controlled melting regime comes from the laboratory study by Ramudu et al. (2016). In this setup, the phase change is only due to heat transfer from a well-mixed turbulent layer in direct contact with the interface. Based on the results, the authors suggest an expression for γ_T, which is significantly higher than that suggested by Jenkins et al. (2010b) and Kader and Yaglom (1972), and with a difference that grows as friction velocity increases (see their figure 18). They also apply their parameterisation to observations from Pine Island Glacier (Stanton et al., 2013). This comparison implicitly assumes that the ice face can be treated as approximately horizontal, rather than sloping. Observations there predict an ablation rate of 14 m year^{-1}. We interpret the data for Pine Island Glacier as currently dissolving, but cannot comment on the turbulent flux regime without more detailed oceanographic context. However, using a shear-controlled melting assumption Ramudu et al. (2016) obtain a melt rate of 98 m year^{-1}. This provides an upper limit of how large the ablation rate would be if the warm waters within the cavity come into direct contact with the ice while experiencing high shear conditions.

4.3.1. Sea ice–Ocean Observations

Near-horizontal ice–ocean interfaces are commonly found under sea ice floes. The base of sea ice is usually rough. The additional effects of wind mixing at the air–ocean interface in leads, and extra shear from sea ice motion relative to the underlying ocean, suggest that the sea ice–ocean boundary layer is dominated by the shear-controlled turbulent flux regime. Basal ablation of the sea ice cover can occur as soon as the atmospheric cooling weakens in summer, so we hypothesise that sea ice ablation is initially characterised by dissolving in the early ablation season. Melting sea ice can be found in cases of rapid warm water advection under the existing sea ice cover, such as the transit of warm

ocean fronts or sea ice moving over a warm mixed layer, storm mixing (Meyer et al., 2017), from the upwelling of warm waters that brings warm water in contact with sea ice (Steele and Morison, 1993), or from intense absorption of solar radiation in the upper ocean.

There are many observations of sea ice–ocean boundary layers, so we will focus on selected key milestones. First, by including stratification effects in an expression from Yaglom and Kader (1974), McPhee et al. (1987) demonstrated how the structure of the boundary layer affects the ablation rate based on observations in the Greenland Sea during a storm in 1984. During the time of observations ocean temperatures in the top part of the water column were below 0 °C. Thus the ice was dissolving, most likely in the shear-controlled regime. The main result of the study is that neglecting the effects of the molecular sublayer on heat and salt transfer leads to an overestimation of ablation.

McPhee (1992) formulated a flux parameterisation proportional to $T_w - T_L(S_w)$, which approximates the interfacial temperature by the freezing temperature of the far-field fluid when calculating the driving temperature difference. This potentially calls for a new definition of the turbulent transfer coefficient, which no longer explicitly describes the integral change of the variable between the interface and the ocean measurement. In this case the bulk Stanton number St_* can be approximated as a constant for measurements under sea ice (see also Appendix B). Based on observations, McPhee et al. (1999) suggested that the use of the complex Re-dependent expressions for turbulent transfer coefficients derived from Kader and Yaglom (1972) is not warranted. However, their use of $T_L(S_w)$ instead of T_i may introduce errors in ablation rate of up to 20% (Notz et al. (2003), their Section 4.2). For details on differences between coefficient and temperature difference definitions, see (Notz et al. (2003), their Section 3.1) and McPhee (2016), their Section 5.3.3, 5.3.5).

It is also important to determine the value of the double diffusion ratio $R = \gamma_T/\gamma_S$ which is determined by the relative efficiency of heat and salt transfer (McPhee, 2008; McPhee et al., 2008). This value has a range of 35–70 based on boundary layer theories (Notz et al., 2003). From observations of false bottoms, Notz et al. (2003) inferred $R = 70$, while Sirevaag (2009), working under rapidly melting multiyear ice pack, measured $R = 33$. However, Keitzl et al. (2016b) suggested that the double diffusion ratio based on parameters measured away from the interface is different from that assessed at the interface. They found $R \approx 83 - 100$ at the interface, and using $R = 33$ leads to an overestimation of ablation by 40%.

The difficulties in obtaining field observations of the ice–ocean boundary layer suggest the potential value of future laboratory and DNS studies with a realistic geometric setup with ice on top of water, and realistic ocean conditions. Studies will benefit from including ocean currents, thus studying the interplay between stratification from melt and shear from currents. DNS modelling will allow for direct calculations of stability criteria described in Section 3 for all interface orientations. In the context of ablation type classification, a set of simultaneous observations from the ocean boundary layer (high-resolution temperature, salinity, and velocity profiles that together provide an assessment of stratification and shear) and basal ablation, made in a range of ice–ocean environments (warm and cold, over a range of water speeds) is urgently needed.

4.4. Stratification effects

The influence of ocean stratification has been studied next to a vertical wall, leading to layered outflows. Sloping surfaces will experience similar effects, scaled for slope angles. First, we discuss the layering effects in the water next to the interface, before focussing on the impact of stratification on shear-controlled turbulent flux regimes.

The stratified ocean environment can guide a meltwater plume to spread horizontally into layers of neutral buoyancy or can create double-diffusion driven intrusions. These effects have been shown in a series of laboratory studies (Section 4.1), and have been applied to

the scale of an ice shelf front (van Heijst, 1987), observed in the ocean (Jacobs et al., 1981; Ohshima et al., 1994; Stephenson et al., 2011), and modelled in an ocean model with glacier termini (e.g., Carroll et al., 2017; Rignot et al., 2016; Sundfjord et al., 2017; Xu et al., 2012, 2013) and on smaller scales (e.g., Ezhova et al., 2017, 2018). Recently, McConnochie and Kerr (2016) and Gayen et al. (2016a) used laboratory studies and complementary DNS modelling to focus on the effect of a salinity gradient on the ablation rate. McConnochie and Kerr (2016) provided a stratification parameter that identifies when stratification starts to affect the flow: a strongly stratified fluid reduces the interface temperature, plume velocity, and, therefore the ablation rate.

The effects of stratification have also been studied in relation to the boundary layer structure at a horizontal interface. In general, stratified boundary layers lead to shorter mixing lengths, shallower velocity boundary layers, and less mixing in the boundary layer (e.g., Turner, 1973; Mahrt, 2014; Malyarenko, 2019). Following on from Martin and Kauffman (1977) for the case of high water temperatures and low ocean velocities, Josberger (1983) predicted the formation of a two-layer system. Steele and Morison (1993) observed that increased local ablation led to increased stratification, shutting off further entrainment of warm waters into the boundary layer. Recent observations of Randelhoff et al. (2014) and Peterson et al. (2017) showed that a shear-controlled formulation and bulk heat transfer coefficient overestimated the heat flux under sea ice in those summer periods where significant stratification is observed under sea ice. Such stratification reduces turbulent fluxes below values predicted by a shear-controlled flux parameterisation that does not account for stratification. Thus a single set of bulk values for γ is not applicable to sea ice modelling in all seasons and there is a need for flexible parameterisations.

Extreme stratification has also been observed in the coastal areas next to a river mouth (Shirasawa and Ingram, 1991a,b). In the Beaufort Sea in early spring the surface ocean layer consists of a 2 m thick layer of fresh run-off water with temperatures above 0 °C, while ocean velocities slowly vary in time (Weingartner et al., 2017). In general, on a large scale in the Arctic Ocean recent ablation of sea ice has increased the upper ocean stratification, further limiting mixing within the boundary layer (McPhee et al., 2009). However, due to a greater area of open water and a thinner more deformable ice cover, the competing effect of wind-driven shear has also increased. The interplay between these effects is complex (e.g. Davis et al., 2016).

In ice shelf cavities, observations of stratification are very limited and diverse. For the Ronne Ice Shelf cavity, Jenkins et al. (2010b) reported ocean temperature in the upper 25 m of the water column, which reflected much variability and a complex boundary layer structure. Kimura et al. (2015) demonstrated that double diffusive staircases developed in the absence of shear, with a much smaller observed ablation rate than the ablation rate generated by shear-controlled flux parameterisations. For the Pine Island Ice Shelf cavity, Stanton et al. (2013) reported low ocean velocities (0.1 m s^{-1}) and stratification within a metre of the interface, leading Dutrieux et al. (2014) to suggest that stratification in the ice–ocean boundary layer limits the heat flux to the interface on basal terraces. Additionally, Kimura et al. (2016) suggested that friction velocity estimates may be affected by boundary layer stratification. Begeman et al. (2018) found a stratified water column in the grounding zone of the Ross Ice Shelf. Water column observations showed double diffusive convection and low ablation rates, and tidal currents were not able to homogenise stratification between an upper layer (within 1 m from the interface) and the mixed layer (3–6.5 m from the interface).

It is not clear whether the molecular sublayer thickness is dependent on ocean stratification in the boundary layer. Currently the only way to include the effects of stratification is to explicitly account for any impact of stratification on turbulence in the boundary layer in ablation parameterisations, based on information from the whole boundary layer. To fully include the impact of stratification on ablation it may be necessary to account for the new (reduced) thickness of the boundary

layer, and the inclusion of the Monin–Obukhov scale to reproduce the shape of the velocity profile (see for example McPhee, 2008; McPhee et al., 2019). In Large Eddy Simulations, the Monin–Obukhov scale has been successfully used to show how stratification reduces the predicted ablation rates in strongly stratified cases (Vreugdenhil and Taylor, 2019). On the scale of the boundary layer models, Jenkins (2016) showed effects of stratification on the current structure beneath the ice shelf base. In cases of gentle slopes, a buoyant Ekman flow can be found with along-slope advection, which maintains the stratification in the boundary layer.

In a complex geophysical setup with any slope direction, the shear in the boundary layer will depend on the net speed, accounting for the sum of different contributions from both turbulence created by ablation (buoyant rising plume), and from external turbulence (tidal mixing, currents).

4.5. Roughness effects

Roughness effects on turbulent fluxes have been studied in theoretical works on shear flow (e.g., Jimenez, 2004) and heat transfer in Rayleigh–Benard convection (c.f. Toppaladoddi et al., 2017; Zhu et al., 2017, and studies therein). The relationship between roughness and turbulence has been studied under sea ice in observations and models (McPhee, 2008; Tsamados et al., 2014). The roughness of an ice shelf base has been indirectly observed through estimates of the friction velocity (Stanton et al., 2013) and directly with echosounders (Nicholls et al., 2006). A series of works for heat fluxes in fully turbulent flows over surfaces with varying roughness were conducted by Kader and Yaglom, based on the theory development by Monin and Yaglom (Kader and Yaglom, 1972, 1977; Monin and Yaglom, 1971; Yaglom and Kader, 1974; for details see Appendix B).

Despite these efforts, the range of possible under-ice roughness values remains unconstrained. Possible effects of multi-scale roughness on the boundary layer structure, and therefore on the ablation rate, have been explored via variation of the drag coefficient in modelling on the whole ice shelf scale (Gwyther et al., 2015). However, interactions and feedbacks between ablation and roughness are likely to exist at a range of scales (Robinson et al., 2017). At the large scale, roughness may be generated by features such as ridges and keels under sea ice and by ice shelf crevasses, each of which can influence the regime under which ablation occurs. At the small scale, the rate of ablation itself is likely to both affect, and be affected by, the local small-scale roughness. This critical interaction between boundary layer structure and roughness has wider implications, such as influencing tidal energy sinks (Padman et al., 2018).

5. Ablation parameterisations in modelling applications

A combination of thermal and turbulent flux regimes creates a spectrum of ablation types: buoyancy-controlled dissolving, shear-controlled dissolving, buoyancy-controlled melting, and shear-controlled melting. In this section we aim to classify existing studies by ablation type, where possible. We examine studies that provide a formulation for the thermodynamic balance at the ice–water interface that determines the rate of ablation. We do not aim to provide a comprehensive list of all work, but to provide representative examples of ablation types. Based on the discussions of Section 4, we define criteria for large-scale investigations that do not resolve the molecular sublayer structure. The criterion for turbulent flux regimes is the inclusion of water velocity in the turbulent transfer coefficient (also described briefly in Magorrian and Wells, 2016). None of the current parameterisations explicitly distinguish regimes of dissolution and melting. Many use the 3-equation formulation with similar treatments of salt and heat fluxes but $\gamma_S \ll \gamma_T$, which should faithfully recreate a dissolving limit. This should also have the potential to transition to a melting-like limit if the thermal driving is very large (Wells, 2008), although the transition to melting is

poorly constrained. It is also not clear whether such turbulent flux laws are accurate in a melting regime, as they do not explicitly account for the dynamics of the fresh, buoyant melt layer in the molecular sublayer at the ice–ocean interface, seen during melting regimes (as discussed in Section 2). Existing parameterisations of thermodynamic balance next to the interface in ice–ocean models can be grouped by the underlying assumptions made in the respective parent studies or observations that were used for fitting coefficients (Fig. 4).

5.1. Models of the boundary layer: Plume and mixed layer models

Plume models are an efficient way to study the ablation of ice. By definition, plume models traditionally use mean values of the plume variables and so do not directly allow the study of details of the boundary layer structure, such as stratification effects within the boundary layer. For ice shelves, plume models are based upon the work of MacAyeal, Jenkins and others (e.g. MacAyeal, 1985; Jenkins, 1991, 2011; Jenkins and Bombosch, 1995; Lane-Serff, 1995). The theory does not apply everywhere (see also Section 4.2 for a discussion of sloping plumes). The effects of rotation and topography were later incorporated in two-dimensional plume modelling (Holland et al., 2007; Holland and Feltham, 2006; Payne et al., 2007; Wilchinsky et al., 2007). All of these models employ the same thermodynamic balance parameterisation from Jenkins (1991), appropriate to shear-controlled ablation (ocean velocity included in the turbulent transfer coefficient). Lazeroms et al. (2018) analysed solutions of a plume model to derive a parameterisation of the basal ablation for ice shelves in 2-D, including variation of the freezing temperature with depth. Pelle et al. (2019) included the plume parameterisation in the PICO model and showed an improvement in the calculation of ablation next to grounding lines.

Plume models have also been applied to submarine ablation of tidewater glaciers. Slater et al. (2016) used a buoyant plume model to show that a single ablation rate scaling is not uniformly applicable to all glaciers, and that the introduction of fjord stratification, for example, leads to higher dependence of ablation rate on discharge. Cowton et al. (2015) demonstrated another way to use a plume model by applying a plume model as a subgrid parameterisation next to an ice face in a fjord. This allowed for a pragmatic use of coarse spatial and temporal resolution. Magorrian and Wells (2016) used a plume model to derive a parameterisation for ablation of tidewater glaciers in a stratified ocean, relevant to cases where the plume is not strongly influenced by subglacial discharge. The results show layered outflows. Jackson et al. (2017) and Beckmann et al. (2018) showed that the application of wider line plume models is more appropriate than buoyant cone models for the simulation of Greenland glaciers. All of these derived parameterisations are implicitly assuming shear-controlled turbulent fluxes (except for the alternative model in the Supplementary Information of Magorrian and Wells, 2016). This is probably acceptable for high plume speeds but becomes more questionable as plume speeds drop below a few centimetres per second.

Another way of simplifying an ocean model, but still forcing the ice–ocean interface with different fluxes, is to use a mixed layer model. As with plume models, the ocean boundary layer is assumed well mixed. This is a computationally inexpensive way to create a more realistic map. For example, Scheduikat and Olbers (1990) applied this concept to the Ross Ice Shelf, representing the ocean cavity as a two-layer or three-layer system. Fluxes between ice and a mixed layer model can be treated explicitly as is done in coupled ice–ocean models (see Petty et al., 2013 and derivatives thereof), or they can be simplified in an ice shelf cavity model (Little et al., 2009).

5.2. Ocean modelling

5.2.1. Ice shelf-ocean models

The general approaches for ice shelf-ocean models were recently reviewed by Dinniman et al. (2016). Here we focus on different approaches to the thermodynamic balance formulation and how they relate to the ablation types.

The majority of the models use the "3-equation balance", as described in Hellmer and Olbers (1989) and Holland and Jenkins (1999) with flux formulations from Jenkins et al. (2001), while some studies simplify the balance by neglecting the heat flux conducted into the ice (e.g., Reese et al., 2018). The use of velocity-dependent turbulent transfer coefficients is common, and with it researchers face the problem of tuning the drag coefficient (Dansereau et al., 2014; Gwyther et al., 2015; Jenkins et al., 2010a; Jourdain et al., 2017) and defining the "mixed layer velocity" value in settings where model resolution may partially resolve the boundary layer (Dansereau et al., 2014; Gwyther et al., 2015). Similar to Slater et al. (2015), Gwyther et al. (2016) impose a low-circulation limit $u_{*min} = 2 \times 10^{-5}$ ms^{-1}. This friction velocity value scales the resulting transfer coefficient value to be close to molecular thermal diffusion, assuming that the flow becomes laminar. A brief summary of the representation of processes in different models can be also found in Asay-Davis et al. (2017), and for a brief summary of γ and the effect of freezing point definitions see Mueller (2014), Chapter 2.

Dansereau et al. (2014) studied the effects of velocity-dependent and velocity-independent transfer coefficients in an idealised cavity shape and for the Pine Island Ice Shelf. They also provide an excellent overview of existing ice shelf models including whether turbulent transport coefficients of Hellmer and Olbers (1989) or Holland and Jenkins (1999) are used. While Hellmer and Olbers (1989) use a transfer coefficient that is independent of ocean velocity, their transfer coefficient can be reconciled with a shear-controlled parameterisation with an assumed, representative, constant flow speed (Timmermann et al., 2002). However, this treatment does not account for the dependency of ablation rate on reduced gravity that is expected in the buoyancy-controlled regime. The results of Dansereau et al. (2014) and Naughten et al. (2018b) show that even within shear-controlled turbulent flux regimes, ablation rate patterns vary and uncertainties remain.

Nakayama et al. (2017) created a regional optimisation study and tuned heat transfer coefficient values for thirteen ice shelves separately in order to bring them closer to observation-based estimates from Rignot et al. (2013). They used a parameterisation in the form of Hellmer and Olbers (1989) and a constant double diffusion ratio yielding heat transfer coefficients ranging from 0.0786×10^{-4} to 15.2×10^{-4} ms^{-1} (for comparison, Hellmer and Olbers (1989) suggested value is 1×10^{-4} ms^{-1}). Clearly some of the higher values reflect additional mixing by ocean currents, while lower values might result from effects of stratification next to the interface. Whilst this inverse approach provides a valuable context on processes driving melt in contemporary conditions, it is not clear how these coefficients reflect the underlying physics and if they will respond appropriately to changing ocean conditions in the future.

The response of ice shelf ablation to higher ocean temperatures has been a key question over the last decades. Holland et al. (2008) showed that an ocean circulation model using a shear-controlled parameterisation suggested a quadratic evolution of ablation with increasing ocean temperatures, because the geostrophic ocean currents are proportional to temperature differences. This result was later used as a simplified boundary condition in ice sheet studies (to be discussed in Section 5.3). In this case the heat flux parameterisation used is proportional to velocity in the mixed layer (corresponding to a shear-controlled regime, rather than buoyancy-controlled), even though the ocean flow in the interior and mixed layer is driven by the buoyancy of the meltwater. The prediction that ablation rates grow nonlinearly with ocean warming is only valid at low tidal velocities (Holland et al., 2008). We note that Figure 1 of Holland et al. (2008) shows how different the existing predictions are depending on the type of study (observations, availability of ocean data close to ice shelf grounding line, ablation rate parameterisation used, type of model used). We would further suggest that, at higher temperatures, such as $T_w = +2$ °C, using a dissolving parameterisation may lead to underestimation of the ablation, as the system is likely to be in transitional state between

melting and dissolving (See Section 2 for details). Further, Little et al. (2009) showed that heat flux towards the interface has a complex relationship with ice shelf morphology and ocean temperatures: not all of the heat available in the mixed layer is spent locally on ablation, and the efficiency of heat flux transfer decreases with increasing ocean temperatures, thus diverging from the quadratic scaling.

5.2.2. Sea Ice–Ocean Models

Models of sea ice–ocean interactions also include a parameterisation of the boundary layer fluxes. For recent reviews on sea ice modelling see Notz (2012) and Notz and Bitz (2016). Here we note that in the state of the art coupled models, such as those coupled to CICE (e.g., Tsamados et al., 2015) and LIM (Vancoppenolle et al., 2009), the heat flux to the sea ice is described with the heat potential formulated in a similar manner to McPhee et al. (2008). Recent advances in sea ice models include a new thermodynamic ice scheme to account for mushy layer thermodynamics (Hunke et al., 2015; Turner and Hunke, 2015). As noted in Feltham and Worster (2000), mushy layer ablation usually occurs by dissolution. Thus we can classify sea ice–ocean models as shear-controlled dissolving but concede that, while we expect this to be the most common type of sea ice ablation, other ablation types are not described by this parameterisation.

5.2.3. Icebergs, ice shelf termini and other applications

The "wall case" solution can be applied to ablation of glacier and ice shelf termini, iceberg sides, and sides of individual sea ice floes. The MITgcm ocean model has been modified (e.g., Sciascia et al., 2013; Xu et al., 2012, 2013) to describe tidewater glacier ablation. These studies showed that ablation rates are sensitive to subglacial water outflow, using velocity-dependent parameterisations for ablation rate. Sciascia et al. (2013) included a dependence on the horizontal velocity, which, in theory, allows for tidal pumping and thereby increased ablation rates if tides are included in the models. For winter conditions, this approach yielded a double cell circulation with detachment of the plume at intermediate depths, analogous to observations in stratified ocean conditions (Jacobs et al., 1981; Stephenson et al., 2011; Straneo and Cenedese, 2015).

The local velocity in the boundary layer is important for parameterising shear-controlled turbulent fluxes and may be affected by different approaches in large-scale models. External velocity sources, such as tidal currents, most likely increase entrainment of ambient waters into the rising plume, thus changing the plume's buoyancy and velocity. We suggest that one role of velocity is as a measure of turbulence in the boundary layer, so defining flow speed from vertical and horizontal components, $\overline{U} = \sqrt{W^2 + U^2}$, rather than just one component may account for all possible mixing in the system, as in Sciascia et al. (2013) and FitzMaurice et al. (2017). The modified approach of Slater et al. (2015), who suggested $\overline{U} = max(\sqrt{W^2 + U^2}, u_{*min})$ which imposed a minimum velocity $u_{*min} = 0.04$ m s^{-1}, is aimed at representing "delicate plumes" not resolved with a model resolution of 5 m. While this may be a first order fix to represent the two turbulent flux regimes, we note that u_{*min} is within the transition range 0.03–0.05 m s^{-1} between buoyancy-controlled and shear-controlled regimes described by McConnochie and Kerr (2017). It is not clear if simply assigning the lower value for u_{*min} will result in an ablation rate value comparable to that calculated by the buoyancy-controlled regime parameterisation. Replacing the value of u_{*min} with the velocity scale appropriate for buoyancy-controlled convection (c.f. Kerr and McConnochie, 2015) is a possible solution for accounting for such background melt, which may be in the buoyancy-controlled regime.

Modelling of icebergs presents an opportunity to test different ablation parameterisations, such as in Stern et al. (2017). Their model employs a velocity-dependent parameterisation for basal ablation. For larger icebergs, basal ablation is described using the parameterisation of Holland and Jenkins (1999), following the approach of previous studies (i.e. Rackow et al., 2017; Silva et al., 2006). But for smaller ice

elements the velocity dependence is decreased from U^1 for a typical ice–ocean parameterisation (e.g. Holland and Jenkins, 1999) to $U^{0.8}$ for basal ablation rate (following a theory of a fully turbulent flow past a finite length plate, e.g. Martin and Adcroft, 2010). For the sides of icebergs, a buoyant convection ablation rate parameterisation is included (an empirical fit to observations, which is only a function of temperature difference).

A similar approach has been tested by FitzMaurice et al. (2017) in a laboratory study. They showed that iceberg sides ablate differently when the buoyant plume is attached to the iceberg surface (lower relative speed between the iceberg and the water) compared to when the plume is detached (higher relative speed). The transition happens when the background ocean flow speed exceeds the plume speed, and the resulting formula for side ablation combines the effects of basal and buoyant ablation. FitzMaurice et al. (2016) and FitzMaurice and Stern (2018) show differences in approaches to modelling icebergs using the 3-equation parameterisation versus the earlier bulk parameterisations, and emphasise the importance of using temperature and velocity data at depth to force the basal ablation of icebergs (and not ambient ocean surface values).

5.3. Simple parameterisations of ablation in ice sheet and glacier modelling

For ice sheet modelling, it is desirable to have efficient parameterisations that can characterise ice ablation without having to resolve the 3-dimensional ocean dynamics, which generally evolve on a faster timescale than the ice sheet. Thus the thermodynamic balance in the form of the 3-equation model is often not included. A common feature of many studies is to use parameterisations based solely on the temperature difference between the ice and the ocean ("temperature forcing"), or depending on the ice shelf draft, or with fixed ablation rates imposed.

The parameterisations are often based on a set of observations away from the interface, a small subset of observations close to the interface, or modelling results at a different scale. The parameterisations encompass whatever conditions were used when diagnosing the parameterisation, and thus inherit the relevant ablation types. The observations have not always been made close to the interface, so the fitted parameterisations also inherit any biases occurring due to variation of conditions between the measurement depth and the ice base. For other recent reviews on ice sheets, we recommend Fyke et al. (2018; their Appendix A lists the relevant papers); Pattyn et al. (2017) provide a review of ice sheet modelling results; Asay-Davis et al. (2017) and Goelzer et al. (2017) summarise methodologies of marine ice sheet modelling; Truffer and Motyka (2016) review on glacier ablation caused by the oceans; and Straneo and Cenedese (2015) review observations and modelling of Greenland fjords.

Complex models on smaller scales are often used to produce simple parameterisations that can be used later in large-scale studies. Thus these larger-scale models are highly dependent on the ablation treatment in the original small-scale detailed studies. Examples of creating simple parameterisations that rely on temperature and subglacier discharge include Xu et al. (2013), which is later used in Rignot et al. (2016), and the quadratic parameterisation of Holland et al. (2008) used in DeConto and Pollard (2016). Both simple parameterisations represent shear-controlled ablation, despite including different power-law relationships, because both are based on Holland and Jenkins (1999). Using simple parameterisations may lead to contrasting biases in the buoyancy-controlled regime (low ocean currents), and in areas with strong tidal flow, unless the parameterisation is directly calibrated to account for this effect.

Temperature-forced basal ablation rates, such as in Martin et al. (2011) and Pollard and Deconto (2012) overestimate present day ablation rates when using γ_T tuned to 3-equation parameterisations, and so a scaling parameter is introduced that decreases ablation rate (and acts in place of the limiting role of salt-diffusion). De Rydt and Gudmundsson (2016) showed that such simple ablation parameterisations
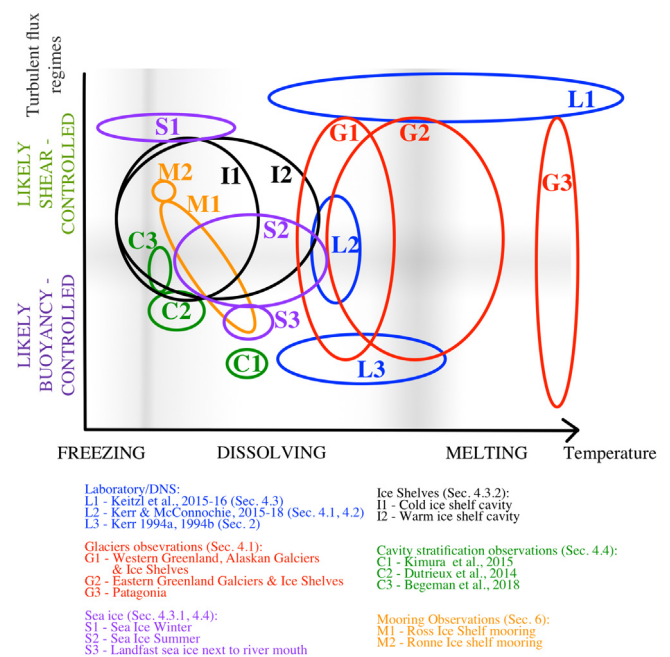

Fig. 5. Schematic diagram of ablation types and suggested ocean conditions that can be found next to different ice types. Existing studies are discussed in Sections 4–5, mooring observations are discussed in Section 6. The straight transition lines (grey shading) indicate that the precise ranges of these transitions remain uncertain. The freezing-dissolving transition occurs roughly at −2 °C; the dissolving-melting transition occurs roughly from −0.5 °C to +5 °C. The turbulent flux regime transition happens at 0.03–0.05 m s^{-1} for vertical walls.

can overestimate the ablation rate by over 40% compared with coupled modelling using a 3-equation parameterisation.

The inconsistencies and absence of consensus in cryospheric modelling approaches is a problem of societal relevance, because projections of sea level rise are sensitive to predicted ice sheet ablation rates. Based on present knowledge of ablation types, ice sheet modelling without realistic representation of the ice–ocean interface and ocean boundary layer can lead to large uncertainties. Coupled ice sheet-ocean models are urgently required. Insights might also be gained from incorporating localised high spatial resolution focused on the ocean boundary layer. In this case models would be able to create more suitable, flexible parameterisations that are able to change with the ocean environment.

5.4. Ablation parameterisation synthesis

In this section we have sought to classify studies by ablation type. Sea ice, ice shelves and Greenland tidewater glaciers are surrounded by different ocean conditions and in Fig. 5 we tentatively sketch possible ablation types for each of these systems. This figure represents a schematic approximation of ablation types experienced by different regions. Current scaling laws make no direct distinction between boundary layer dynamics for melting and dissolving. As temperature measurements of ocean conditions are much more common than turbulence observations, we may consider the location on the abscissa of Fig. 5 as more robust. However, the transition point between melting and dissolving is presently poorly constrained, and Fig. 5 presents our best approximation for the location of this transition. Along the turbulence scale, our classification is binary: in some cases fluxes can be positively identified as either shear-controlled or buoyancy-controlled. For most glaciers and ice shelves we assume that both turbulent flux regimes exist. Despite all of these limitations, we provide an overview of which ablation types are well studied and observed.

6. Ablation types under ice shelf bases: application to observations

As has been described in Sections 2 and 3, details that determine the ablation type are confined to sublayers close to the ice–water interface. Unfortunately it is very difficult to make observations at this scale in a geophysical setup. However, we can use existing time series of ocean observations below the ice to force the parameterisations and compare to observed ablation rates. Whilst this requires making several simplifying assumptions, it provides an initial step towards evaluating the ablation type theory using real observations and revealing dynamical insight into the changing regimes.

In this section we compare two observational datasets (from the Ross Ice Shelf and from the Ronne Ice Shelf cavities) and attempt to calculate the value of Re_c, as described in Eq. (5) of Section 3, that could be applicable for the ice shelf cavity environment. The observations were chosen as they are the only long-term moorings that include all four observations necessary: temperature, salinity, velocity and ablation rate.

6.1. The Ross Ice Shelf cavity observations

The Coulman High oceanographic mooring was located to the east of Ross Island about 7 km south of the ice shelf front (171°E, 77°S) and deployed from 2011 to 2015 (Arzeno et al., 2014; Stewart et al., 2019). The top set of instruments had a CTD-logger, a Seabird Electronics SBE 37-IM MicroCAT, at 226 metres below sea level (mbsl) or about 5.5 m below the base of the ice shelf. Next, a current meter, Nortek Aquadopp IM6000 was located at 228 mbsl or at 7.5 m below the base of the ice shelf. The current meter measured velocities and temperature. The latter was calibrated against the more accurate MicroCAT record during well-mixed periods in winter when both instruments were in the same layer. For a full description of the deployment see Stewart (2017).

The ablation rate was calculated by Stewart (2017) from an Upward Looking Sounder (Tritech PA-500 acoustic altimeter), located at 232 mbsl or 12.5 m below the base of the ice shelf. After post-processing, Stewart (2017) was able to confidently produce a long-term trend and low-frequency variability of the ablation record.

6.2. The Ronne Ice Shelf cavity observations

The Site 5c mooring was located at S 80°14'.22, W 54°42'.51, 18 km west of the coast of Berkner Island, and some 300 km from the nearest ice front. At that site the ice was 740 m thick, and the instruments nearest the base of the ice shelf were 24 m from the ice–ocean interface at the time of deployment (January 2015). That cluster of instruments consisted of an Aquadopp 3000 m "Deep Water" current meter, a Seabird Electronics SBE 37 Microcat and an RBR Duo, recording conductivity and temperature. Here we use year-long records of water speed, temperature and salinity from the data provided by the Aquadopp and Microcat. Also deployed at this site was an autonomous phase-sensitive radio echosounder (ApRES) (Nicholls et al., 2015), which yielded a contemporaneous record of basal ablation. In this study, we use low-pass filtered versions of the time series of melt rates and ocean conditions, with a cut-off of 48 h.

6.3. Calculating sublayer Reynolds number Re_δ

In order to calculate local $Re_\delta = \frac{W\delta}{\nu}$ according to Eq. (5) and the definitions provided in Wells and Worster (2008), two parameters are needed. Wells and Worster (2008) defined the molecular sublayer thickness as the distance δ where the turbulent heat flux exceeds 10% of the mean conductive heat flux (Wells and Worster, 2008, formula 6.34). We cannot calculate this value directly. Instead, we estimate $\delta \sim h_c$, using the compositional boundary layer thickness h_c from Kerr and McConnochie (2015). h_c is easily calculated from the observations

(i.e. calculation of interface values from formulae 4.1 and 4.2 of Kerr and McConnochie (2015), then using their formula 2.15). For a direct comparison to Wells and Worster (2008), the value of Re_δ should be proportionally scaled (in a similar way to formulae (6.37, 6.43) of Wells and Worster, 2008), to reflect the ratio of the sublayer thicknesses. Determining the ratio of h_c to δ is not currently possible, but they should differ only by a factor of order one.

Second, the mean velocity U parallel to the boundary (called W in Wells and Worster, 2008), was used as a substitute value for the velocity U_δ at the boundary of the sublayer thickness. We cannot reliably predict the velocity value at the sublayer boundary edge as we cannot predict δ or h_c. If there is also an ambient velocity in the ocean cavity as well as a buoyancy-driven boundary layer flow, it is possible there could be distinct velocity scales, so that the measured horizontal velocity of the boundary layer (U) might not be representative of U_δ (the substitution $W \sim W_\delta$ was made based on scaling arguments in the absence of ambient flow in Wells and Worster, 2008).

Next, the effects of stratification and position of the instrument need to be discussed. We denote the velocity value measured by the instrument as U_m. In neutrally stratified conditions with tidally driven flow, most of the change of the velocity is expected to occur close to the interface, and so we assume the value in the middle of the boundary layer is close to the value at the edge of the boundary layer. However, in highly stratified conditions, the change in the boundary layer may be more gradual, or some step changes may appear. We cannot quantify these effects with certainty, without a full time series of vertical velocity profiles, which is not available. Instead, we use the value that is measured by instruments away from the interface ($U \sim U_m$) and discuss possible errors arising from changing stratification.

Two CTD casts are available from the Ross Ice Shelf mooring, representing low-ablation and high-ablation conditions (Fig. 6a and c). Based on them, we can interpret the depth of the mixed layer ≈ 10 m in summer and ≈ 30 m in winter during the period of observation. The site experiences a seasonal signal in the record next to the ice shelf base (Fig. 7) related to inflow of Antarctic Surface Water (AASW) into the cavity. The ADCP located 7.5–14.5 m away from the interface (the distance increasing over 5 years as the interface moved up due to ice ablation) is likely to be outside of the boundary layer in summer for at least part of the time series, and in the boundary layer in winter. Hence, in summer conditions we expect that U_m probably overestimates the mean velocity U, and in winter conditions U_m is likely to be close to U. Thus, summer Re values are overestimated, and winter Re values are close to those calculated with U.

A CTD cast is available from the mooring under the Ronne Ice Shelf, shown as the mean of several casts taken within a few-hour period (Fig. 6b and d). The cast shows a well-mixed layer 20 m thick, while the instruments are located about 24 m away from the interface. This site experiences no clear seasonality in the measured ocean conditions (Fig. 8a), so we expect that the cast is representative of the whole year of observations. The instrument is likely to be just outside the boundary layer and stratification in the boundary layer is small. Thus U_m is likely to be close to the value at the edge of the boundary layer. Nonetheless the value of U_m may not be entirely representative of U.

6.4. Available ablation rate parameterisations

With both datasets, it is possible to use ocean observations to predict ablation rate, as formulated by various parameterisations, and compare it with the measured ablation rate. As was discussed in Sections 4.3.1 and 5.2, many of the parameterisations have similar dynamical forms, and so we only choose 5 formulations that are significantly different from each other (see Table 1 for finer details of the parameterisations chosen).

First, we hypothesise that the effects of compositional buoyancy, as discussed in Section 4.4, may be affecting the ice shelf observations. Kerr and McConnochie (2015, KM 2015 for convenience) is the
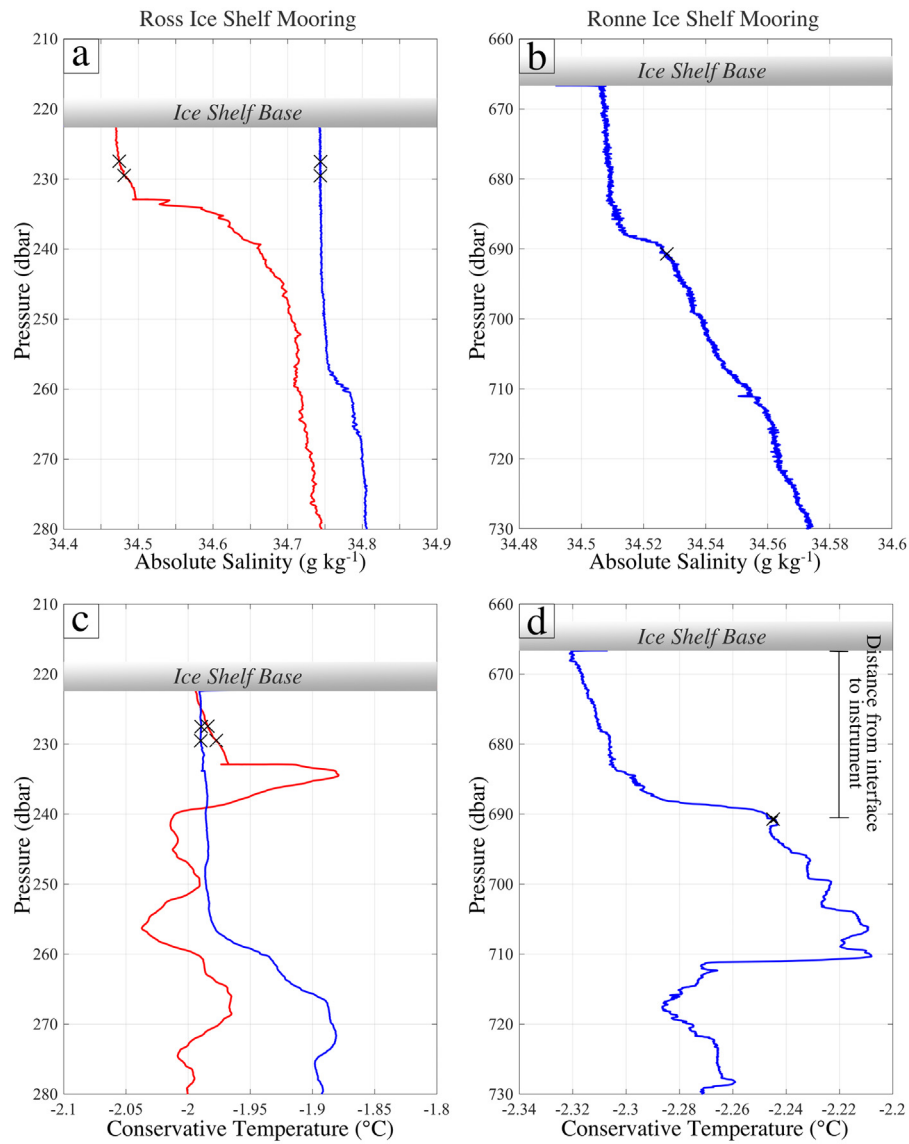
Fig. 6. Salinity at (a) Ross and (b) Ronne Ice Shelf (2015–16) mooring locations and temperature at (c) Ross and (d) Ronne Ice shelf mooring locations. Crosses represent instrument positions that are used for the analysis. The profiles were taken before mooring deployments in November 2010 (blue) and January 2011 (red) from the Ross Ice Shelf mooring location, and in January 2015 from the Ronne Ice Shelf mooring location.

Table 1
Ablation rate parameterisations used in Figs. 7 and 8. For description of studies see Section 6.4.

Citation	Notes on modifications and parameters chosen.
KM 2015 (Kerr and McConnochie, 2015)	Solved as formulae (2.23, 2.24) from the paper. Pressure-dependent freezing point added, as formulated in HJ 1999. Buoyancy-controlled regime is hypothesised.
HO 1989 (Hellmer and Olbers, 1989)	No modifications.
N 2003 (Notz et al., 2003)	Pressure-dependent freezing point added, as formulated in HJ 1999. Friction velocity solved as formulated in HJ 1999. $R = 70$ $\Gamma_T = 0.0135$
HJ 1999 (Holland and Jenkins, 1999)	Heat flux through the solid is always included (eq. 31, melting case only). Surface temperature of ice shelf is assumed -25 °C. Stability parameter is set to 1.
J 2010 (Jenkins et al., 2010b)	Recommended values based on observation: $\Gamma_S = 0.00031$ $\Gamma_T = 0.011$ $C_d = 0.0097$

Fig. 7. An overview of ablation regimes in the Ross Ice Shelf cavity. (a) In situ temperature (blue) and ocean velocity (red) records. (b) Ablation rate predicted by parameterisations (Table 1) and the observed ablation rate. (c) Coefficient r of turbulent flux regimes: $r > 0$ m year^{-1} is shear-controlled, and $r < 0$ m year^{-1} is buoyancy-controlled. Shading indicates buoyancy-controlled periods. (d) Reynolds number Re (see Eq. (5)) calculated for the boundary layer. Shading for the same periods as in (c), i.e. when the system is buoyancy-controlled. Black line indicates a suggested critical value of 20. Note that the Ross Ice Shelf mooring data is plotted for 4 years, compared with 1 year for the Ronne.

only formulation of buoyancy-controlled ablation that we are aware of. While the base of an ice shelf is nearly horizontal, and hence a "buoyancy-driven" parameterisation developed for a wall is not necessarily applicable, we follow KM 2015 and trial its applicability here to understand the role of buoyancy-controlled ablation. Curiously, Kerr and McConnochie (2015) found that their scaling law for a vertical wall provided reasonable predictions of the magnitude of ice shelf and iceberg ablation, despite the discrepancy in slope. A possible interpretation is that significant boundary roughness may be providing small-scale steep sloping surfaces that would facilitate buoyancy-driven flow. The video record from the Ross Ice Shelf mooring showed no frazil attached to ice shelf base (Rack et al., 2012), and we do not expect that the Ronne Ice Shelf mooring has a frazil layer attached to the ice shelf base either. A large-scale slope approximation is available for the Ross Ice Shelf mooring (Stewart, 2017), but the slope of 0.22° does not support direct application of McConnochie and Kerr (2018) either.

For the second parameterisation, we choose Hellmer and Olbers (1989, abbreviated as HO 1989), who assume a constant velocity of 0.15 m s^{-1}, which is slightly larger than the mean observed velocity in both datasets (0.12 m s^{-1} for the Ross Ice Shelf and 0.09 m s^{-1} for the Ronne Ice Shelf). Third, we select Notz et al. (2003, abbreviated as N 2003) as the synthesis of observations under sea ice. We note that the ratio of double diffusion (R) is not settled. We use $R = 70$, as recommended in Notz et al. (2003), which is a value in the middle of the possible interval (see Section 4.3.1). Next, we choose Holland and Jenkins (1999, abbreviated as HJ 1999) as the most commonly used ice shelf-ocean parameterisation, using simplifications for the stability parameter from McPhee et al. (1987) as described in Holland and Jenkins (1999). Finally, Jenkins et al. (2010b, abbreviated as J 2010) is selected because this expression is tuned to ice shelf-ocean observations.
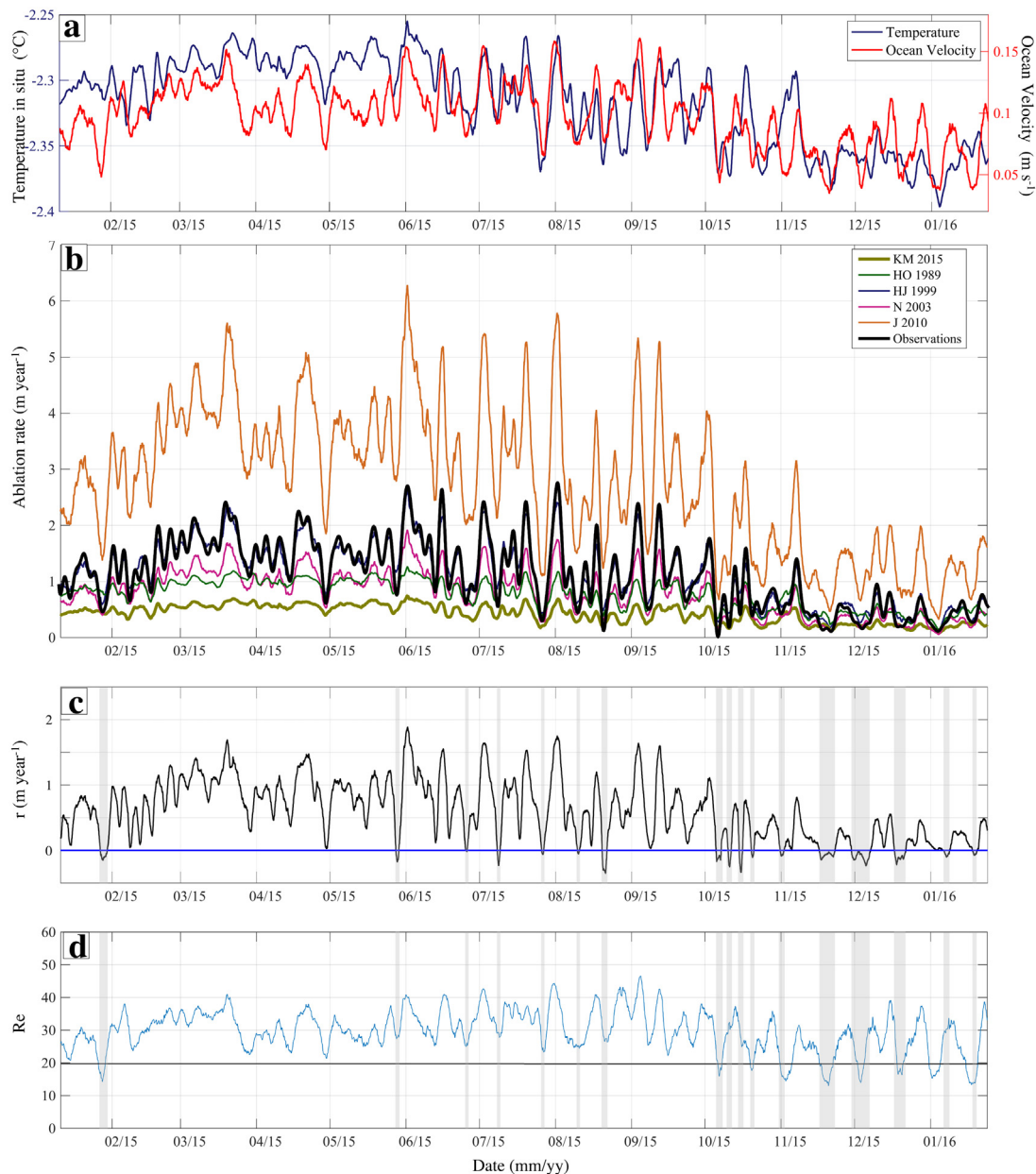
Fig. 8. An overview of ablation regimes in the Ronne Ice Shelf cavity, same as Fig. 7. (a) In situ temperature (blue) and ocean velocity (red) records. (b) Ablation rate predicted by parameterisations (Table 1) and the observed ablation rate. (c) Coefficient r of turbulent flux regimes: $r > 0$ m year^{-1} is shear-controlled, and $r < 0$ m year^{-1} is buoyancy-controlled. Shading indicates buoyancy-controlled periods. (d) Reynolds number Re (see Eq. (5)) calculated for the boundary layer. Shading is for the same periods as in (c). Black line indicates a suggested critical value 20. Note that the Ronne Shelf mooring data is plotted for 1 year, compared with 4 years for the Ross.

Owing to different methods and temporal resolution used in the ablation rate measurement, Ross and Ronne records were smoothed differently from each other. The Ross Ice Shelf mooring ablation rate predictions, temperature and current records are smoothed with a 30-day running mean (Fig. 7a and b). For Re values, we provide 30-day and 3-day running means (Fig. 7d). The Ronne Ice Shelf mooring ablation rate predictions, observed temperature, current and ablation records and Re values are smoothed with a 3-day running mean (Fig. 8).

The ablation parameterisations could potentially be tuned to observed ablation rates. J 2010 slightly overestimates ablation rates when applied to a different location in the same cavity (Fig. 8b), and significantly overestimates ablation rates in the Ross Ice Shelf mooring, especially in warmer periods (Fig. 7b). Tuning J 2010 to the Ross Ice Shelf mooring has been accomplished by Stewart (2017) for a short-term deployment of ApRES in 2014. The RMS error was successfully reduced during "well-mixed" periods in winter (temperature observations 15 and 20 m away from the interface are within 0.05 °C of each

other). The tuned parameterisation produces ablation rates values close to HJ 1999 (mean difference is 0.05 m year^{-1}). Differences between locations can potentially be interpreted as boundary roughness changes (e.g., Stewart, 2017). The seasonal overestimation of parameterisations indicates changes in the ocean boundary layer affecting the ablation rate parameterisations.

We hypothesise that the seasonal signal in the Ross Ice Shelf mooring is related to a shift in turbulent flux regimes. Following the description in Section 5, we choose one velocity-dependent parameterisation as shear-controlled, and one velocity-independent parameterisation as buoyancy-controlled.

If R is kept constant, all velocity-dependent parameterisations are scaled versions of one another, and all describe the same ablation type. Based on Fig. 4, we suggest that the velocity-dependent parameterisation (HJ 1999) we are using already include some effects of stratification, keeping in mind that the stratification effects were tuned

to observations made during a storm under sea ice, i.e. still describing shear-controlled dissolving (McPhee et al., 1987). Thus, choosing any particular velocity-dependent parameterisation will not be representative of different boundary layer processes, even though they would appear to scale. We retain HJ 1999 parameterisation without changes as it has been commonly used in many studies and is representative of shear-controlled dissolving.

We choose to incorporate KM 2015 parameterisation as a high estimate of ablation in a buoyancy-controlled regime, assuming that small-scale roughness is sufficient to generate local regions of steep slope. Accounting for small-scale roughness would lower the predicted ablation rates by $(\sin \varphi)^{2/3}$ versus the prediction for a vertical wall with $\sin \varphi = 1$ (i.e. for $\varphi > 60°$ the scaling coefficients is >0.9).

Using the parameterisations of HJ 1999 and KM 2015, we suggest that the turbulent flux regime switches from shear-controlled to buoyancy-controlled, when the observed ablation rate is closer to the prediction of one parameterisation or the other. Using the coefficient $r = \left| \dot{w}_{obs} - \dot{w}_{KM2015} \right| - \left| \dot{w}_{obs} - \dot{w}_{HJ99} \right|$ m year^{-1} we suggest that $r > 0$ m year^{-1} might be interpreted as closer to shear-controlled dissolving, and $r < 0$ m year^{-1} is buoyancy-controlled (subject to a potentially prohibitive assumption about the slope of roughness on the ice shelf boundary discussed above). Such values of $r < 0$ m year^{-1} could alternatively be simply indicative of a poor quality of fit to the HJ 1999 parameterisation for a shear-controlled boundary layer, perhaps as a result of neglecting the impact of a strong stratification. We will describe these cases as buoyancy-controlled below, but these caveats and alternative interpretations should be borne in mind The Ross Ice Shelf r values are plotted using the observed ablation rate and a 30-day running mean of the predicted rate (Fig. 7c). The Ronne Ice Shelf r values are plotted using a 3-day running mean of both observed and predicted ablation rates (Fig. 8c).

6.5. Implications for the ice shelf ablation parameterisation

First, based on the boundary layer structure and the coefficient r we suggest that for most of the year the Ronne Ice Shelf mooring site was under a regime of shear-controlled dissolving ($r > 0$ m year^{-1} in Fig. 8c). While ocean velocity is low, weak stratification in the boundary layer (Fig. 6b and d) is likely to have a weak effect in the velocity profile, allowing the shear to be transported closer to the interface. Thus while $r > 0$ m year^{-1} we interpret Re values as those descriptive of a shear-controlled regime. We somewhat arbitrarily choose $Re_c = 20$ as the Reynolds stability critical number, which ensures all events with $r > 0$ m year^{-1} in Fig. 8 describe the shear-controlled regime. There are also short periods when $r < 0$ m year^{-1} (shaded grey in Fig. 8 c), and Re is below 20 (shading in Fig. 8d for the same periods as in c).

Next, the Ross Ice Shelf mooring experiences a clear seasonal cycle. In winter, r is above 0 m year^{-1}, and we classify the system as shear-controlled. Indeed, the low observed ablation rates suggest weak stratification in the boundary layer (Fig. 6a and c, blue). Also, the location of the Ross Ice Shelf mooring, next to an active polynya, leads to eddy activity in winter (Årthun et al., 2013) and increased mixing in the boundary layer. In summer, high local ablation leads to increased stratification and thinning of the boundary layer (Fig. 6(a) and (c), red), and r is below 0 m year^{-1}. We suggest that the system can then be described as buoyancy-controlled. If this is the case, the same Re_c value should be applicable to this site as to the Ronne Ice Shelf, as we are using the same methodology to calculate it. While there is no clear signal of Re crossing a threshold, during summers Re values tend to be lower than in winter, and dip below Re_c. We interpret the signal in the Ross Ice Shelf mooring as a seasonal inflow of AASW creating the stratification in the ocean boundary layer, perhaps between the interface and the instrument position. The ablation rates in summer are lower than predicted by the shear-controlled parameterisation due to 'shielding' effects similar to those presented in Section 4.4.

We note that a lot of variation in Re might be explained by the available observations only acting as a proxy, rather than a direct measurement. First, U_δ is likely to have less variability than U_m due to the reduction in turbulent fluctuations close to the interface. Second, using $\delta \sim h_c$ may lead to additional inaccuracy. Third, the effects of surface roughness are not included in KM2015, and the impact of roughness on C_d in the shear-controlled regime may be debated. Lastly, as discussed in Section 6.3, summer Re values are likely to be overestimated, and winter Re values are likely underestimated. Thus a Re calculated with fewer assumptions may have shown a stronger seasonal signal in the record from the Ross Ice Shelf Mooring.

Despite these major constraints from the types of observations, some preliminary conclusions can be noted. Both sites may be described as dissolving, as the ocean temperatures stay below 0 °C. The Ross Ice Shelf mooring likely experiences both types of turbulent flux regimes, while the Ronne Ice Shelf mooring is dominated by the shear-controlled regime, potentially with occasional short pulses of buoyancy-controlled dynamics. Perhaps surprisingly, the data are suggestive that the application of theory of turbulent flux regimes (i.e. calculation of Re_c) by Wells and Worster (2008), developed for a vertical wall, approximately captures the transitions for a mostly horizontal ice shelf base, as seen through the use of r to compare observed ablation rates with those calculated from parameterisations in each regime. Whilst there is no firm evidence, taken alongside the good comparison to ice shelf melt rates predicted by Kerr and McConnochie (2015), one possible interpretation is that these ice shelves all have steep small scale roughness, although other effects may be important. Notably, the transition to a putative buoyancy-controlled regime suggested here could simply be a result of a poor fit of a shear-controlled parameterisation, and the better agreement with the scaling of Kerr and McConnochie (2015) could be co-incidental. Alternatively, this change could be suggestive of a strong impact of stratification on the shear driven boundary layer in summer.

7. Summary and future research priorities

Ablation types are affected by two thermal and multiple turbulent flux regimes, including the thermodynamics of melting and dissolving, and buoyancy- and shear-controlled turbulent fluxes.

Next to vertical, sloping and horizontal interfaces, different ablation types have been commonly observed. Cold ice shelf cavities and sea ice interfaces, commonly horizontal or slightly sloping, are typically classified as shear-controlled dissolving. Glaciers and warm cavity ice shelves can be in contact with warm waters, suggesting they may be in a melting regime either currently or under further future warming. Additional effects of stratification and surface roughness affect the boundary layer processes, thus determining which ablation type is present. We have reviewed the existing regimes captured in model parameterisations. Modelling approaches differed based on temporal and spatial resolutions, and interface orientation (e.g., iceberg sides and ice shelves). None of the current parameterisation explicitly distinguish ablation types. Simplified parameterisations inherit the ablation type of the underlying observations or a more complex parameterisation, thus are tuned to a specific set of ocean conditions.

Our analysis of mooring data under ice shelves suggests that both shear- and buoyancy-controlled dynamics could be relevant during different seasons and synoptic events. The transitions between regimes are broadly consistent with a shear-controlled regime for larger values of a Reynolds number for the molecular sublayer, and a buoyancy-controlled regime for smaller Reynolds number. However, explanations for outliers and variability between these regimes cannot be explained by the limited available observational data. Curiously, the buoyancy-controlled ablation theory of Kerr and McConnochie (2015) for vertical ice faces seems to better capture ablation rates during many of the periods with low Reynolds number, despite it being applied here to shelves with very shallow mean slope. A potential explanation could

be the significance of small scale variations in slope over local roughness, although this requires more detailed observations to test and explore.

Models that focus on regional differences and future projections may benefit from flexible parameterisations to account for these differences. Turbulent flux regimes in the ice–ocean boundary layer need to be considered if the impact on ablation of changes in circulation and stratification are to be captured. Seasonal and synoptic changes in background circulation, atmospheric forcing and the stratification are not universal, but common enough to incorporate in modelling of ice–ocean ablation. These processes, often large-scale, are already incorporated in ocean models, but not accounted for directly in the class of ablation parameterisations that do not account for changes to the ocean circulation.

The importance of thermal regimes varies regionally. Arctic and Antarctic sea ice and cold cavity ice shelves are in conditions that currently imply dissolving. In areas where Circumpolar Deep Water comes into contact with warm cavity ice shelves and warm surface waters come into contact with sea ice and ice shelves, the temperatures may lie above the dissolving limit, and in the melting regime. The melting solution is also already relevant to glacier termini in warm fjords and will become more applicable to ice shelves in future warming scenarios. Such warming near ice shelves could result from either regional warming of a given water mass, or from a changing pattern of advection of existing water masses. We also stress that the dynamics of the turbulent melting regime is not well characterised, and it is unclear exactly how much warming is needed to shift into a melting regime. Currently available ablation parameterisations have been largely based on calibration in the dissolution regime. The transition to melting has not been fully tested but could become important in the future.

If a future study aims to include regional differences and stratification effects in the results, there is no existing parameterisation that correctly describes all possible conditions, and piecewise transitions may be needed between different regimes. Other possible solutions include choosing a parameterisation of the ablation type which best fits the given initial ice shelf cavity conditions. However, such a study would subject the outcome to preconceived assumptions about cavity conditions.

Future research on the transitions between ablation types could focus on quantifying slope effects, acknowledging the challenges from laboratory constraints on the Reynolds number and the difficulties of making observations of small-scale processes in the field. Currently, the prudent approach that uses net boundary layer speed (i.e. buoyancy + tides + geostrophic) may be applicable to calculation of Re and division of regimes. However, it is necessary to characterise the transitions more precisely if accurate predictions of current and future states of the ice–ocean interface are to be achieved.

We realise that direct applicability of the classification that relies on processes that happen on such small scales is challenging. However, we hope that this is a step in the direction of reduced uncertainty in the ice–ocean ablation.

Based on the presented review, several areas for future research are recommended below:

1. Targeted high-resolution observations are needed in a range of environments. Suggested observations might include: in the ice shelf cavity, under fast ice, or in the lab with an ice roof and imposed currents, with realistic water temperatures spanning the range −2 to +10 °C.
2. Small-scale modelling, such as DNS and LES (noting that LES does not fully resolve the turbulent dynamics), may be a first step in studying transitions in different environments.
3. Possible applications of buoyancy-controlled ablation parameterisations under shallow slopes and horizontal interfaces such as the ice shelf base need to be researched further.
4. All ablation type transitions need to be better constrained.

5. Additional effects of roughness of all scales on the boundary layer structure should be studied.
6. Effects of stratification in the ocean boundary layer on the ablation rate should be researched further.
7. Future research on ice ablation needs to be directed at melting regimes that are suggested theoretically but remain observationally underconstrained, and can be expected to grow in relevance in nature with continued warming of the ocean.

Declaration of competing interest

The authors declare that they have no known competing financial interests or personal relationships that could have appeared to influence the work reported in this paper.

Acknowledgements

Appendix A. Nomenclature

Typical denominations for water, ice, and interface vary in past literature. In order to avoid confusion between studies, we have adapted all notations to a common framework for this study.

a, b and c — empirical constants for pressure-dependent freezing point

c_{ice} — specific heat capacity of ice

c_w — specific heat capacity of water

C_d — drag coefficient

D — molecular salt diffusivity

F_S — salt flux through compositional sublayer of width h_c

$g' = \frac{g(\rho_\infty - \rho_i)}{\rho_\infty}$ — reduced gravity based on density difference

h_c — compositional sublayer thickness (as defined in Kerr and McConnochie, 2015)

L — specific latent heat of fusion

Nu_z — local Nusselt number

p — pressure

Pr — Prandtl number

q — heat flux through the boundary layer

Q_T^{ice} — heat flux through ice

Q_T^{Latent} — latent heat

Q_T^w — heat flux through water (interface — ocean grid cell)

Q_S^{Brine} — net salt flux from ablation or freezing

Q_S^w — turbulent heat flux through water (interface — ocean grid cell)

$R = \gamma_T / \gamma_S$ — double diffusion ratio

Ra_δ – boundary layer Rayleigh number – buoyancy stability criteria

Ra_z — Local Rayleigh number at distance z from origin of the flow.

Re_δ – Reynolds number – shear stability criteria

Re_c — Critical Reynolds number

Ri_* — convective Richardson number

S_i — interface salinity

S_{ice} — ice salinity

S_w — water salinity at the edge of the boundary layer

Sc — Schmidt number

$St = \frac{Nu}{RePr}$ — Stanton number

St_* — bulk Stanton number

T_i — interface temperature

T_{ice} — ice temperature

Table B.1
Transfer coefficient definitions.

Nomenclature Citation	Name used	Definition and further details
B (Owen and Thomson, 1963)	Stanton number	$B = \frac{1}{\alpha}\left(\frac{u_\tau h}{v}\right)^{-0.45} Pr^{-0.8}$ h — sublayer thickness u_τ - "characteristic velocity of eddying fluid" in the sublayer, or friction velocity α — constant for roughness (between 0.45 and 0.7) Assumptions made: (1) 2-layer model (2) heat transfer is mainly confined to a sublayer where it is controlled by molecular conductivity.
c_h (Monin and Yaglom, 1971)	Stanton number	The heat transfer coefficient (Stanton number): $c_h = \frac{q_o}{c_p \rho U (T_0 - T_1)}$ The modified heat transfer coefficient: $C_h = \frac{q_o}{c_p \rho U_m (T_0 - T_m)} = \frac{c_h}{1 - \Delta}$ $\Delta = \frac{T_m - T_1}{T_0 - T_1}$ T — concentration of passive admixture. In case of temperature and salinity, assumption of passivity is doubtful due to buoyancy forces (Sec. 5.7) T_0 — interface value T_1 — value at the boundary layer thickness (eq. 5.80) T_m — bulk temperature U — typical velocity scale of the flow U_m — average bulk velocity (Sec. 5.5) q_o — heat flux directed from the interface Theory assumes (Sec. 5.7 (Monin and Yaglom, 1971; Kader and Yaglom, 1972; Yaglom and Kader, 1974)): (1) Turbulent heat and mass transfer are much greater than the molecular transfer in turbulent outer flow (2) The viscous and molecular diffusivity sublayers, and the buffer sublayer provide negligible contribution to the bulk velocity, bulk temperature and bulk concentration. No measurements of the sublayer of molecular thermal diffusivity were available, but it was shown that the scaling $c_h \sim Pr^{-2/3}$ at $Pr \gg 1$ gives a good description of available data. (their formula 5.86').
c_h (Kader and Yaglom, 1972)	Stanton number	Follows definitions of c_h and C_h of Monin and Yaglom (1971). For universal function of Pr a 2-layer model of boundary layer is used with a molecular sublayer and fully turbulent layer. In the molecular sublayer both the molecular and turbulent transfer are considered.
C_h (Kader and Yaglom, 1972)	Modified Stanton number (based on bulk measurements)	For smooth walls in pipes and water best fit is (formula 30): $C_h = \frac{(C_f/2)^{1/2}}{2.12\ln\left(C_f^{1/2} Re\right) + 12.5 Pr^{2/3} + 2.12\ln Pr - 10.1}$ $C_f = 2\left(\frac{u_*}{U}\right)^2$ — skin friction coefficient u_* — friction velocity U — typical velocity scale of the flow
C_h (Yaglom and Kader, 1974)	Modified Stanton number (based on bulk measurements)	For a completely rough wall at high Re (their formula 22): $C_h = \frac{(C_f/2)^{1/2}}{2.12\ln\left(\frac{L}{h}\right)^{1/2} + 0.55(Pr^{2/3}-0.2)h_+^{1/2} + 10 - \frac{3.2}{(1-\eta_1)^2} + 6.6(C_f/2)^{1/2}}$ L — pipe radius / half-width of channel / boundary layer thickness $h_+ = \frac{h u_*}{v}$ h — mean height of roughness $\eta_1 = h/L$ — relative roughness height
C_h (Kader and Yaglom, 1977)	Modified Stanton number (based on bulk measurements)	For a wall with parallel roughness ridges (their formula 14): $C_h = \frac{(C_f/2)^{1/2}}{3.2 h_+^{1/4}(Pr^{2/3}+0.3) - 2.12\ln\eta_1 + 4 - \frac{3.2}{(1-\eta_1)^2} + 6.7(C_f/2)^{1/2}}$ Nomenclature are the same as in (Yaglom and Kader, 1974).

T_w — water temperature at the edge of the boundary layer

ΔT — temperature difference, or driving temperature (definitions vary between studies)

ΔS — salinity difference (definitions vary between studies)

T_L — freezing temperature of water of given salinity

U — mean horizontal velocity of the boundary layer

U_m — measured velocity

u_* — friction velocity

u_{*min} — minimum friction velocity to avoid zero ablation

W — mean vertical (or alongslope) velocity of the boundary layer

$\dot{w}$ — interface velocity, or ablation rate of ice (positive for ice ablation)

z — height above leading edge

γ_T^{ice} — heat transfer coefficient through ice

γ_T and γ_S — transfer coefficients of heat and salt through water, appropriately describing change of scalar over the chosen distance.

Γ_T and Γ_S — nondimensional transfer coefficients of heat and salt through water

δ — molecular sublayer thickness

κ — thermal diffusivity of water

κ_{ice} — molecular thermal diffusivity of ice

v — kinematic viscosity

ρ_i — interface density

ρ_{ice} — ice density

ρ_w — water density

φ — slope angle ($\varphi = 0$ is horizontal, $\varphi = 90$ is vertical)

Table B.1 (*continued*).

Nomenclature Citation	Name used	Definition and further details
Φ (McPhee et al., 1987)	Nondimensional change in temperature from the interface to the level z	Definition: $\Phi = \int_z^0 \frac{u_* dz}{K_h}$ Connection to other: $\Phi = \frac{1}{St}$ Resulting expression: $\Phi = \Phi_{turb} + \Phi_{mole}$ $\Phi_{turb} = \frac{1}{k} \ln\left(\frac{u_* \xi_N \eta_*^2}{f z_0} \right) + \frac{1}{2\xi_N \eta_*} - \frac{1}{k}$ $\Phi_{mole} = 1.57 \left(\frac{u_* z_0}{\nu} \right)^{0.5} Pr^{0.67} - 6$ z_0 — Roughness elements scale u_* — friction velocity ξ_N — dimensionless constant η_* — stability parameter f — Coriolis parameter k — Von Karman constant K_h — heat diffusivity Assumptions made: (1) 2-layer models are essential, with most of the change in scalar quantities occurring within the laminar/transition sublayer. (2) Buoyancy effects are important in high ablation conditions (3) Effects of rotation are needed for evaluation of the boundary layer thickness.
c_H (McPhee, 1992; McPhee et al., 1999)	Heat transfer coefficient (turbulent Stanton number)	Definition: $c_H = \frac{\langle w'T' \rangle_0}{u_{*0} \delta T}$ $\delta T = T_{mixedlayer} - T_L(S_{mixedlayer})$ u_{*0} — friction velocity at the boundary $\langle w'T' \rangle_0$ — the kinematic heat flux at the interface Observations showed that $St_* = \frac{\langle w'T' \rangle_0}{u_{*0} \delta T}$ and $Re_* = f\left(\frac{u_{*0} z_0}{\nu} \right)$ do not follow Yaglom and Kader (1974), and so it is assumed that $c_H = const$ is a better choice. Not clear if requirements of Yaglom and Kader (1974) are satisfied when Re_* is calculated for all observations ($h_+ = \frac{hu_*}{\nu} > 100$, closely spaced roughness elements).
α_h (Notz et al., 2003; McPhee et al., 2008; McPhee, 2016)	Turbulent exchange coefficients; Interface exchange coefficient	Definition: $\alpha_H = \frac{\langle w'T' \rangle_0}{u_*(T_{mixedlayer} - T_L(S_{interface}))}$ Notz et al. (2003) use u_* for the friction velocity throughout the paper.
St_* (Notz et al., 2003; McPhee et al., 2008; McPhee, 2016)	Bulk exchange coefficients; Stanton Number	$St_* = \frac{\langle w'T' \rangle_0}{u_{*0}(T_{mixedlayer} - T_L(S_{mixedlayer}))}$ Notz et al. (2003) use u_* throughout the paper.
γ [m s^{-1}] ((Hellmer and Olbers, 1989)	Turbulent heat exchange coefficient	Constant value ($\gamma = 10^{-4}$ m s^{-1}) that assumes ocean velocity of 15 cm s^{-1}.
γ [m s^{-1}] (Jenkins, 1991)	Turbulent transfer velocity	Based on C_h (Kader and Yaglom, 1972). $\gamma = \frac{K^{1/2} U}{2.12 \ln\left(K^{\frac{1}{2}} Re \right) + 12.5 Pr^{2/3} - 8.68}$ U — mean plume velocity K — dimensionless drag coefficient
γ [m s^{-1}] (Jenkins and Bombosch, 1995)	Heat Transfer coefficient	Definition: $\gamma = \frac{Nu K_T}{\Delta_T}$ Δ_T — Boundary layer thickness K_T — Molecular diffusivity Nu — Nusselt number, "which represents the increase in the heat flux through the outer part of the boundary layer caused by turbulence" Based on C_h (Kader and Yaglom, 1972). Used expression: $\gamma = \frac{K^{1/2} U}{2.12 \ln\left(K^{\frac{1}{2}} Re \right) + 12.5 Pr^{2/3} - 9}$ K — dimensionless drag coefficient
γ [m s^{-1}] (Grosfeld et al., 1997)	Coefficient of turbulent heat flux	Constant value $\gamma = 4.2 \times 10^{-5}$ m s^{-1}. The value comes from the heat transfer coefficient (2.8×10^{-4}) and ocean velocity 0.15 m s^{-1}.
γ [m s^{-1}] (Holland and Jenkins, 1999)	Thermal exchange velocity	Definition: $\gamma = \frac{Nu \kappa_M^T}{h}$ Nu — Nusselt number "that describes nonlinearity of temperature profile and variable diffusivity in the boundary layer" κ_M^T — thermal diffusivity adjacent to the ice–ocean interface h — boundary layer thickness Used expression: $\gamma = \frac{u_*}{\Gamma_{mole} + \Gamma_{turb}}$, $\Gamma_{mole} = 12.5 Pr^{2/3} - 6$, $\Gamma_{turb} = \frac{1}{k} \ln\left(\frac{u_* \xi_N \eta_*^2}{f h_\nu} \right) + \frac{1}{2\xi_N \eta_*} - \frac{1}{k}$. h_ν — Thickness of viscous sublayer Definitions follow McPhee et al. (1987). Assume $\eta_* = 1$.
Γ (Jenkins et al., 2010b)	Dimensionless transfer coefficient	Similar to St_* (McPhee et al., 2008). Constant values of Γ and C_d are recommended based on observations under Ronne ice shelf.

Table B.1 (*continued*).

Nomenclature Citation	Name used	Definition and further details
γ [m s^{-1}] (Jenkins et al., 2010b)	Dimensioned transfer velocity	Similar to γ (Jenkins, 1991)
γ (Kimura et al., 2016)	Nondimensional exchange coefficients of the heat and salt transfer through the boundary layer	Assume that molecular contributions dominate the exchange. $\gamma_T = 1.6 \times 10^{-2}$ $\gamma_S = 4.4 \times 10^{-4}$
γ (Kerr and McConnochie, 2015)	Constant	Describes relationship $Nu = \gamma Ra^{1/3}$, derived from laboratory experiments

Appendix B

As the understanding of heat and salt transfer in the ocean boundary layer evolved, the definition of transfer coefficient changed. This not only includes nomenclature, but differences in what this variable represents and how it is defined. Here we briefly track the evolution of definitions. We use notations and names of parameters as authors used in each study to outline the difference between assumed variables (e.g., velocity U may represent bulk velocity in the boundary layer, far-field velocity, mean plume velocity) (see Table B.1).

References

Alley, K.E., Scambos, T.A., Siegfried, M.R., Fricker, H.A., 2016. Impacts of warm water on Antarctic ice shelf stability through basal channel formation. Nat. Geosci. 9, 290–293. http://dx.doi.org/10.1038/ngeo2675.

Årthun, M., Holland, P.R., Nicholls, K.W., Feltham, D.L., 2013. Eddy-driven exchange between the open ocean and a sub–ice shelf cavity. J. Phys. Oceanogr. 43, 2372–2387. http://dx.doi.org/10.1175/JPO-D-13-0137.1.

Arzeno, I.B., Beardsley, R.C., Limeburner, R., Owens, B., Padman, L., Springer, S.R., Stewart, C.L., Williams, M.J.M., 2014. Ocean variability contributing to basal melt rate near the ice front of Ross Ice Shelf, Antarctica. J. Geophys. Res. Ocean. 119, 4214–4233. http://dx.doi.org/10.1002/2014JC009792.

Asay-Davis, X.S., Jourdain, N.C., Nakayama, Y., 2017. Developments in simulating and parameterizing interactions between the Southern ocean and the Antarctic Ice Sheet. Curr. Clim. Chang. Rep. 3, 316–329. http://dx.doi.org/10.1007/s40641-017-0071-0.

Beckmann, J., Perrette, M., Ganopolski, A., 2018. Simple models for the simulation of submarine melt for a Greenland glacial system model. Cryosphere 12, 301–323. http://dx.doi.org/10.5194/tc-12-301-2018.

Begeman, C.B., Tulaczyk, S.M., Marsh, O.J., Mikucki, J.A., Stanton, T.P., Hodson, T.O., Siegfried, M.R., Powell, R.D., Christianson, K., King, M.A., 2018. Ocean stratification and low melt rates at the ross ice shelf grounding zone. J. Geophys. Res. Ocean 123, 7438–7452. http://dx.doi.org/10.1029/2018JC013987.

Blanchard-Wrigglesworth, E., Barthélemy, A., Chevallier, M., Cullather, R., Fučkar, N., Massonnet, F., Posey, P., Wang, W., Zhang, J., Ardilouze, C., Bitz, C.M., Vernieres, G., Wallcraft, A., Wang, M., 2017. Multi-model seasonal forecast of Arctic sea-ice: forecast uncertainty at pan-arctic and regional scales. Clim. Dyn. 49, 1399–1410. http://dx.doi.org/10.1007/s00382-016-3388-9.

Cape, M.R., Straneo, F., Beaird, N., Bundy, R.M., Charette, M.A., 2019. Nutrient release to oceans from buoyancy-driven upwelling at Greenland tidewater glaciers. Nat. Geosci. 12, 34–39. http://dx.doi.org/10.1038/s41561-018-0268-4.

Carroll, D., Sutherland, D.A., Curry, B., Nash, J.D., Shroyer, E.L., Catania, G.A., Stearns, L.A., Grist, J.P., Lee, C.M., de Steur, L., 2018. Subannual and seasonal variability of atlantic-origin waters in two adjacent west Greenland Fjords. J. Geophys. Res. Ocean 123, 6670–6687. http://dx.doi.org/10.1029/2018JC014278.

Carroll, D., Sutherland, D.A., Shroyer, E.L., Nash, J.D., Catania, G.A., Stearns, L.A., 2017. Subglacial discharge-driven renewal of tidewater glacier fjords. J. Geophys. Res. Ocean 122, 6611–6629. http://dx.doi.org/10.1002/2017JC012962.

Cenedese, C., Gatto, V.M., 2016a. Impact of a localized source of subglacial discharge on the heat flux and submarine melting of a tidewater glacier: A laboratory study. J. Phys. Oceanogr. 46, 3155–3163. http://dx.doi.org/10.1175/JPO-D-16-0123.1.

Cenedese, C., Gatto, V.M., 2016b. Impact of two plumes' interaction on submarine melting of tidewater glaciers: A laboratory study. J. Phys. Oceanogr. 46, 361–367. http://dx.doi.org/10.1175/JPO-D-15-0171.1.

Cowton, T.R., Slater, D.A., Sole, A., Goldberg, D., Nienow, P., 2015. Modeling the impact of glacial runoff on fjord circulation and submarine melt rate using a new subgrid-scale parameterization for glacial plumes. J. Geophys. Res. Ocean 120, 796–812. http://dx.doi.org/10.1002/2014JC010324.

Craven, M., Warner, R.C., Galton-Fenzi, B.K., Herraiz-Borreguero, L., Vogel, S.W., Allison, I., 2014. Platelet ice attachment to instrument strings beneath the Amery Ice Shelf, East Antarctica. J. Glaciol. 60, 383–393. http://dx.doi.org/10.3189/2014JoG13J082.

Dallaston, M.C., Hewitt, I.J., Wells, A.J., 2015. Channelization of plumes beneath ice shelves. J. Fluid Mech. 785, 109–134. http://dx.doi.org/10.1017/jfm.2015.609.

Dansereau, V., Heimbach, P., Losch, M., 2014. Simulation of subice shelf melt rates in a general circulation model: Velocity-dependent transfer and the role of friction. J. Geophys. Res. Ocean 119, 1765–1790. http://dx.doi.org/10.1002/2013JC008846.

Davis, P.E.D., Jenkins, A., Nicholls, K.W., Brennan, P.V., Abrahamsen, E.P., Heywood, K.J., Dutrieux, P., Cho, K., Kim, T., 2018. Variability in basal melting beneath pine island ice shelf on weekly to monthly timescales. J. Geophys. Res. Ocean 123, 8655–8669. http://dx.doi.org/10.1029/2018JC014464.

Davis, P.E.D., Lique, C., Johnson, H.L., Guthrie, J.D., 2016. Competing effects of elevated vertical mixing and increased freshwater input on the stratification and sea ice cover in a changing Arctic ocean. J. Phys. Oceanogr. 46, 1531–1553. http://dx.doi.org/10.1175/JPO-D-15-0174.1.

Davis, P.E.D., Nicholls, K.W., 2019. Turbulence observations beneath Larsen C Ice Shelf, Antarctica. J. Geophys. Res. Ocean. 2019JC015164. http://dx.doi.org/10.1029/2019JC015164.

De Rydt, J., Gudmundsson, G.H., 2016. Coupled ice shelf-ocean modeling and complex grounding line retreat from a seabed ridge. J. Geophys. Res. Earth Surf. 121, 865–880. http://dx.doi.org/10.1002/2015JF003791.

DeConto, R.M., Pollard, D., 2016. Contribution of Antarctica to past and future sea-level rise. Nature 531, 591–597. http://dx.doi.org/10.1038/nature17145.

Depoorter, M.A., Bamber, J.L., Griggs, J.A., Lenaerts, J.T.M., Ligtenberg, S.R.M., van den Broeke, M.R., Moholdt, G., 2013. Calving fluxes and basal melt rates of Antarctic ice shelves. Nature 502, 89–92. http://dx.doi.org/10.1038/nature12567.

Dinniman, M., Asay-Davis, X., Galton-Fenzi, B.K., Holland, P.R., Jenkins, A., Timmermann, R., 2016. Modeling ice shelf/ocean interaction in Antarctica: A review. Oceanography 29, 144–153. http://dx.doi.org/10.5670/oceanog.2016.106.

Dutrieux, P., Stewart, C., Jenkins, A., Nicholls, K.W., Corr, H.F.J.J., Rignot, E., Steffen, K., 2014. Basal terraces on melting ice shelves. Geophys. Res. Lett. 41, 5506–5513. http://dx.doi.org/10.1002/2014GL060618.

Ezhova, E., Cenedese, C., Brandt, L., 2017. Dynamics of a turbulent buoyant plume in a stratified fluid: An idealized model of subglacial discharge in Greenland fjords. J. Phys. Oceanogr. 47, 2611–2630. http://dx.doi.org/10.1175/JPO-D-16-0259.1.

Ezhova, E., Cenedese, C., Brandt, L., 2018. Dynamics of three-dimensional turbulent wall plumes and implications for estimates of submarine glacier melting. J. Phys. Oceanogr. 48, 1941–1950. http://dx.doi.org/10.1175/JPO-D-17-0194.1.

Feltham, D.L., Worster, M.G., 2000. Similarity solutions describing the melting of a mushy layer. J. Cryst. Growth 208, 746–756. http://dx.doi.org/10.1016/S0022-0248(99)00456-X.

FitzMaurice, A., Cenedese, C., Straneo, F., 2017. Nonlinear response of iceberg side melting to ocean currents. Geophys. Res. Lett. 44, 5637–5644. http://dx.doi.org/10.1002/2017GL073585.

FitzMaurice, A., Stern, A.S., 2018. Parameterizing the basal melt of tabular icebergs. Ocean Model 130, 66–78. http://dx.doi.org/10.1016/j.ocemod.2018.08.005.

FitzMaurice, A., Straneo, F., Cenedese, C., Andres, M., 2016. Effect of a sheared flow on iceberg motion and melting. Geophys. Res. Lett. 43, 12, 520–12, 527. http://dx.doi.org/10.1002/2016GL071602.

Fyke, J., Sergienko, O., Löfverström, M., Price, S., Lenaerts, J.T.M., 2018. An overview of interactions and feedbacks between ice sheets and the earth system. Rev. Geophys. 56, 361–408. http://dx.doi.org/10.1029/2018RG000600.

Gade, H.G., 1979. Melting of ice in sea water: A primitive model with application to the Antarctic ice shelf and icebergs. J. Phys. Oceanogr. 9, 189–198. http://dx.doi.org/10.1175/1520-0485(1979)009<0189:MOIISW>2.0.CO;2.

Gayen, B., Griffiths, R.W., Kerr, R.C., 2016b. Simulation of convection at a vertical ice face dissolving into saline water. J. Fluid Mech. 798, 284–298. http://dx.doi.org/10.1017/jfm.2016.315.

Gayen, B., Mondal, M., Griffiths, R.W., 2016a. Effects of stratification on the dissolution of a vertical ice-face. In: 20th Australasian Fluid Mechanics Conference. Perth, Australia.

Gladish, C.V., Holland, D.M., Holland, P.R., Price, S.F., 2012. Ice-shelf basal channels in a coupled ice/ocean model. J. Glaciol. 58, 1227–1244. http://dx.doi.org/10.3189/2012JoG12J003.

Goelzer, H., Robinson, A., Seroussi, H., van de Wal, R.S.W., 2017. Recent progress in Greenland ice sheet modelling. Curr. Clim. Chang. Rep. 3, 291–302. http://dx.doi.org/10.1007/s40641-017-0073-y.

Grosfeld, K., Gerdes, R., Determann, J., 1997. Thermohaline circulation and interaction between ice shelf cavities and the adjacent open ocean. J. Geophys. Res. 102, 15595. http://dx.doi.org/10.1029/97JC00891.

Grossmann, S., Lohse, D., 2000. Scaling in thermal convection: a unifying theory. J. Fluid Mech. 407, S0022112099007545. http://dx.doi.org/10.1017/S0022112099007545.

Gwyther, D.E., Cougnon, E.A., Galton-Fenzi, B.K., Roberts, J.L., Hunter, J.R., Dinniman, M.S., 2016. Modelling the response of ice shelf basal melting to different ocean cavity environmental regimes. Ann. Glaciol. 57, 131–141. http://dx.doi.org/10.1017/aog.2016.31.

Gwyther, D.E., Galton-Fenzi, B.K., Dinniman, M.S., Roberts, J.L., Hunter, J.R., 2015. The effect of basal friction on melting and freezing in ice shelf-ocean models. Ocean Model 95, 38–52. http://dx.doi.org/10.1016/j.ocemod.2015.09.004.

Gwyther, D.E., Spain, E.A., King, P., Guihen, D., Williams, G.D., Evans, E., Cook, S., Richter, O., Galton-Fenzi, B.K., Coleman, R., 2020. Cold ocean cavity and weak basal melting of the sørsdal ice shelf revealed by surveys using autonomous platforms. J. Geophys. Res. Oceans 125, http://dx.doi.org/10.1029/2019jc015882.

Hattermann, T., Nøst, O.A., Lilly, J.M., Smedsrud, L.H., 2012. Two years of oceanic observations below the Fimbul Ice Shelf, Antarctica. Geophys. Res. Lett. 39, http://dx.doi.org/10.1029/2012GL051012.

Hatton, D.C., Woods, A.W., 2007. Compositional controls on melting and dissolving a salt into a ternary melt. Proc. R. Soc. A Math. Phys. Eng. Sci. 463, 1211–1229. http://dx.doi.org/10.1098/rspa.2007.1819.

Hatton, D.C., Woods, A.W., 2008. Diffusion-controlled dissolution of a binary solid into a ternary liquid with partially molten zone formation. Proc. R. Soc. A Math. Phys. Eng. Sci. 464, 1615–1637. http://dx.doi.org/10.1098/rspa.2007.0241.

Hellmer, H.H., Kauker, F., Timmermann, R., Determann, J., Rae, J., 2012. Twenty-first-century warming of a large Antarctic ice-shelf cavity by a redirected coastal current. Nature 485, 225–228. http://dx.doi.org/10.1038/nature11064.

Hellmer, H.H., Olbers, D.J.J., 1989. A two-dimensional model for the thermohaline circulation under an ice shelf. Antarct. Sci. 1, 325–336. http://dx.doi.org/10.1017/S0954102089000490.

Herraiz-Borreguero, L., Allison, I., Craven, M., Nicholls, K.W., Rosenberg, M.A., 2013. Ice shelf/ocean interactions under the Amery Ice Shelf: Seasonal variability and its effect on marine ice formation. J. Geophys. Res. Ocean 118, 7117–7131. http://dx.doi.org/10.1002/2013JC009158.

Herraiz-Borreguero, L., Coleman, R., Allison, I., Rintoul, S.R., Craven, M., Williams, G.D., 2015. Circulation of modified Circumpolar Deep Water and basal melt beneath the Amery Ice Shelf, East Antarctica. J. Geophys. Res. Ocean 120, 3098–3112. http://dx.doi.org/10.1002/2015JC010697.

Holland, P.R., Feltham, D.L., 2006. The effects of rotation and ice shelf topography on frazil-laden ice shelf water plumes. J. Phys. Oceanogr. 36, 2312–2327. http://dx.doi.org/10.1175/JPO2970.1.

Holland, P.R., Feltham, D.L., Jenkins, A., 2007. Ice shelf water plume flow beneath Filchner-Ronne Ice Shelf, Antarctica. J. Geophys. Res. 112, C05044. http://dx.doi.org/10.1029/2006JC003915.

Holland, D.M., Jenkins, A., 1999. Modeling thermodynamic ice–ocean interactions at the base of an ice shelf. J. Phys. Oceanogr. 29, 1787–1800. http://dx.doi.org/10.1175/1520-0485(1999)029<1787:MTIOIA>2.0.CO;2.

Holland, P.R., Jenkins, A., Holland, D.M., 2008. The response of ice shelf basal melting to variations in ocean temperature. J. Clim. 21, 2558–2572. http://dx.doi.org/10.1175/2007JCLI1909.1.

Hunke, E.C., Lipscomb, W.H., Turner, A.K., Jeffery, N., Elliott, S., 2015. CICE: the Los Alamos Sea Ice Model Documentation and Software User ' s Manual LA-CC-06-012.

Huppert, H.E., 1989. Phase changes follwing the initiation of a hot turbulent flow over a cold solid surface. J. Fluid Mech. 198, 293–319.

Huppert, H.E., Josberger, E.G., 1980. The melting of ice in cold stratified water. J. Phys. Oceanogr. http://dx.doi.org/10.1175/1520-0485(1980)010<0953:TMOIIC>2.0.CO;2.

Huppert, H.E., Kerr, R.C., Hallworth, M.A., 1984. Heating or cooling a stable compositional gradient from the side. Int. J. Heat Mass Transf. 27, 1395–1401. http://dx.doi.org/10.1016/0017-9310(84)90066-8.

Huppert, H.E., Sparks, R.S., 1988. Melting the roof of a chamber containing a hot, turbulently convecting fluid. J. Fluid Mech. 188, 107–131. http://dx.doi.org/10.1017/S0022112088000655.

Huppert, H.E., Turner, J.S., 1980. Ice blocks melting into a salinity gradient. J. Fluid Mech. 100, 367–384. http://dx.doi.org/10.1017/S0022112080001206.

Huppert, H.E., Turner, J.S., 1981. Double-diffusive convection. J. Fluid Mech. 106, 299. http://dx.doi.org/10.1017/S0022112081001614.

Jackson, R.H., Shroyer, E.L., Nash, J.D., Sutherland, D.A., Carroll, D., Fried, M.J., Catania, G.A., Bartholomaus, T.C., Stearns, L.A., 2017. Near-glacier surveying of a subglacial discharge plume: Implications for plume parameterizations. Geophys. Res. Lett. 44, 6886–6894. http://dx.doi.org/10.1002/2017GL073602.

Jackson, R.H., Straneo, F., 2016. Heat, salt, and freshwater budgets for a glacial Fjord in Greenland. J. Phys. Oceanogr. 46, 2735–2768. http://dx.doi.org/10.1175/JPO-D-15-0134.1.

Jacobs, S.S., Gordon, A.L., Ardai, J.L., 1979. Circulation and melting beneath the ross ice shelf. Science 203, 439–443. http://dx.doi.org/10.1126/science.203.4379.439.

Jacobs, S.S., Huppert, H.E., Holdsworth, G., Drewry, D.J., 1981. Thermohaline steps induced by melting of the Erebus Glacier Tongue. J. Geophys. Res. 86, 6547. http://dx.doi.org/10.1029/JC086iC07p06547.

Jenkins, A., 1991. A one-dimensional model of ice shelf-ocean interaction. J. Geophys. Res. 96, 20671. http://dx.doi.org/10.1029/91JC01842.

Jenkins, A., 2011. Convection-driven melting near the grounding lines of ice shelves and tidewater glaciers. J. Phys. Oceanogr. 41, 2279–2294. http://dx.doi.org/10.1175/JPO-D-11-03.1.

Jenkins, A., 2016. A simple model of the ice shelf–ocean boundary layer and current. J. Phys. Oceanogr. 46, 1785–1803. http://dx.doi.org/10.1175/JPO-D-15-0194.1.

Jenkins, A., Bombosch, A., 1995. Modeling the effects of frazil ice crystals on the dynamics and thermodynamics of ice shelf water plumes. J. Geophys. Res. 100, 6967. http://dx.doi.org/10.1029/94JC03227.

Jenkins, A., Dutrieux, P., Jacobs, S.S., McPhail, S.D., Perrett, J.R., Webb, A.T., White, D., 2010a. Observations beneath Pine Island Glacier in West Antarctica and implications for its retreat. Nat. Geosci. 3, 468–472. http://dx.doi.org/10.1038/ngeo890.

Jenkins, A., Hellmer, H.H., Holland, D.M., 2001. The role of meltwater advection in the formulation of conservative boundary conditions at an ice–ocean interface. J. Phys. Oceanogr. 31, 285–296. http://dx.doi.org/10.1175/1520-0485(2001)031<0285:TROMAI>2.0.CO;2.

Jenkins, A., Nicholls, K.W., Corr, H.F.J., 2010b. Observation and parameterization of Ablation at the base of Ronne Ice Shelf, Antarctica. J. Phys. Oceanogr. 40, 2298–2312. http://dx.doi.org/10.1175/2010JPO4317.1.

Jimenez, J., 2004. Turbulent flows over rough walls. Annu. Rev. Fluid Mech. 36, 173–196. http://dx.doi.org/10.1146/annurev.fluid.36.050802.122103.

Josberger, E.G., 1983. Sea ice melting in the marginal ice zone. J. Geophys. Res. 88, 2841. http://dx.doi.org/10.1029/JC088iC05p02841.

Josberger, E.G., Martin, S., 1981. A laboratory and theoretical study of the boundary layer adjacent to a vertical melting ice wall in salt water. J. Fluid Mech. http://dx.doi.org/10.1017/S0022112081002450.

Jourdain, N.C., Mathiot, P., Merino, N., Durand, G., Le Sommer, J., Spence, P., Dutrieux, P., Madec, G., 2017. Ocean circulation and sea-ice thinning induced by melting ice shelves in the amundsen sea. J. Geophys. Res. Ocean 122, 2550–2573. http://dx.doi.org/10.1002/2016JC012509.

Kader, B.A., Yaglom, A.M., 1972. Heat and mass transfer laws for fully turbulent wall flows. Int. J. Heat Mass Transf. 15, 2329–2351. http://dx.doi.org/10.1016/0017-9310(72)90131-7.

Kader, B.A., Yaglom, A.M., 1977. Turbulent heat and mass transfer from a wall with parallel roughness ridges. Int. J. Heat Mass Transf. 20, 345–357. http://dx.doi.org/10.1016/0017-9310(77)90156-9.

Keitzl, T., 2015. Turbulent Enhancement of the Melt Rate At an Ice-Ocean Interface. Max Planck Institute for Meteorology.

Keitzl, T., Mellado, J.P., Notz, D., 2016a. Impact of thermally driven turbulence on the bottom melting of ice. J. Phys. Oceanogr. 46, 1171–1187. http://dx.doi.org/10.1175/JPO-D-15-0126.1.

Keitzl, T., Mellado, J.P., Notz, D., 2016b. Reconciling estimates of the ratio of heat and salt fluxes at the ice–ocean interface. J. Geophys. Res. Ocean 121, 8419–8433. http://dx.doi.org/10.1002/2016JC012018.

Kerr, R.C., 1994a. Dissolving driven by vigorous compositional convection. J. Fluid Mech. 280, 287. http://dx.doi.org/10.1017/S0022112094002934.

Kerr, R.C., 1994b. Melting driven by vigorous compositional convection. J. Fluid Mech. 280, 255–285. http://dx.doi.org/10.1017/S0022112094002922.

Kerr, R.C., McConnochie, C.D., 2015. Dissolution of a vertical solid surface by turbulent compositional convection. J. Fluid Mech. 765, 211–228. http://dx.doi.org/10.1017/jfm.2014.722.

Kimura, S., Jenkins, A., Dutrieux, P., Forryan, A., Naveira Garabato, A.C., Firing, Y., 2016. Ocean mixing beneath Pine Island Glacier ice shelf, West Antarctica. J. Geophys. Res. Ocean. 121, 8496–8510. http://dx.doi.org/10.1002/2016JC012149.

Kimura, S., Nicholls, K.W., Venables, E., 2015. Estimation of ice shelf melt rate in the presence of a thermohaline staircase. J. Phys. Oceanogr. 45, 133–148. http://dx.doi.org/10.1175/JPO-D-14-0106.1.

Kobs, S., Holland, D.M., Zagorodnov, V., Stern, A., Tyler, S.W., 2014. Novel monitoring of Antarctic ice shelf basal melting using a fiber-optic distributed temperature sensing mooring. Geophys. Res. Lett. 41, 6779–6786. http://dx.doi.org/10.1002/2014GL061155.

Lane-Serff, G.F., 1995. On meltwater under ice shelves. J. Geophys. Res. Ocean 100, 6961–6965. http://dx.doi.org/10.1029/94JC03244.

Langhorne, P.J., Hughes, K.G., Gough, A.J., Smith, I.J., Williams, M.J.M., Robinson, N.J., Stevens, C.L., Rack, W., Price, D., Leonard, G.H., Mahoney, A.R., Haas, C., Haskell, T.G., 2015. Observed platelet ice distributions in Antarctic sea ice: An index for ocean-ice shelf heat flux. Geophys. Res. Lett. 42, 5442–5451. http://dx.doi.org/10.1002/2015GL064508.

Lazeroms, W.M.J., Jenkins, A., Hilmar Gudmundsson, G., Van De Wal, R.S.W., 2018. Modelling present-day basal melt rates for Antarctic ice shelves using a parametrization of buoyant meltwater plumes. Cryosphere 12, 49–70. http://dx.doi.org/10.5194/tc-12-49-2018.

Little, C.M., Gnanadesikan, A., Oppenheimer, M., 2009. How ice shelf morphology controls basal melting. J. Geophys. Res. Ocean 114, C12007. http://dx.doi.org/10.1029/2008JC005197.

Liu, X., 2018. Modeling the effect of ross ice shelf melting on the southern ocean in quasi-equilibrium. Cryosph 12, 3033–3044. http://dx.doi.org/10.5194/tc-12-3033-2018.

Liu, Y., Moore, J.C., Cheng, X., Gladstone, R.M., Bassis, J.N., Liu, H., Wen, J., Hui, F., 2015. Ocean-driven thinning enhances iceberg calving and retreat of Antarctic ice shelves. Proc. Natl. Acad. Sci. 112, 3263–3268. http://dx.doi.org/10.1073/pnas.1415137112.

MacAyeal, D.R., 1985. Evolution of Tidally Triggered Meltwater Plumes below Ice Shelves. pp. 133–143. http://dx.doi.org/10.1029/ar043p0133.

Magorrian, S.J., Wells, A.J., 2016. Turbulent plumes from a glacier terminus melting in a stratified ocean. J. Geophys. Res. Ocean 121, 4670–4696. http://dx.doi.org/10.1002/2015JC011160.

Mahrt, L., 2014. Stably stratified atmospheric boundary layers. Annu. Rev. Fluid Mech. 46, 23–45. http://dx.doi.org/10.1146/annurev-fluid-010313-141354.

Malyarenko, A., 2019. Ice-ocean boundary layer—Part 2: Variability. In: Encyclopedia of Ocean Sciences. Elsevier, pp. 166–174. http://dx.doi.org/10.1016/B978-0-12-409548-9.11487-3.

Malyarenko, A., Robinson, N.J., Williams, M.J.M., Langhorne, P.J., 2019. A wedge mechanism for summer surface water inflow into the ross ice shelf cavity. J. Geophys. Res. Ocean. 1–19. http://dx.doi.org/10.1029/2018JC014594.

Mankoff, K.D., Straneo, F., Cenedese, C., Das, S.B., Richards, C.G., Singh, H., 2016. Structure and dynamics of a subglacial discharge plume in a Greenlandic fjord. J. Geophys. Res. Ocean 121, 8670–8688. http://dx.doi.org/10.1002/2016JC011764.

Martin, T., Adcroft, A.J., 2010. Parameterizing the fresh-water flux from land ice to ocean with interactive icebergs in a coupled climate model. Ocean Model. 34, 111–124. http://dx.doi.org/10.1016/j.ocemod.2010.05.001.

Martin, S., Kauffman, P., 1977. An experimental and theoretical study of the turbulent and laminar convection generated under a horizontal ice sheet floating on warm salty water. J. Phys. Oceanogr. http://dx.doi.org/10.1175/1520-0485(1977)007<0272:AEATSO>2.0.CO;2.

Martin, M.A., Winkelmann, R., Haseloff, M., Albrecht, T., Bueler, E., Khroulev, C., Levermann, A., 2011. The potsdam parallel ice sheet model (PISM-PIK) - Part 2: Dynamic equilibrium simulation of the Antarctic ice sheet. Cryosphere 5, 727–740. http://dx.doi.org/10.5194/tc-5-727-2011.

Maykut, G.A., Untersteiner, N., 1971. Some results from a time-dependent thermodynamic model of sea ice. J. Geophys. Res. 76, 1550–1575. http://dx.doi.org/10.1029/jc076i006p01550.

McConnochie, C.D., Kerr, R.C., 2016. The effect of a salinity gradient on the dissolution of a vertical ice face. J. Fluid Mech. 791, 589–607. http://dx.doi.org/10.1017/jfm.2016.62.

McConnochie, C.D., Kerr, R.C., 2017. Testing a common ice–ocean parameterization with laboratory experiments. J. Geophys. Res. Ocean 122, 5905–5915. http://dx.doi.org/10.1002/2017JC012918.

McConnochie, C.D., Kerr, R.C., 2018. Dissolution of a sloping solid surface by turbulent compositional convection. J. Fluid Mech. 846, 563–577. http://dx.doi.org/10.1017/jfm.2018.282.

McPhee, M.G., 1992. Turbulent heat flux in the upper ocean under sea ice. J. Geophys. Res. 97, 5365. http://dx.doi.org/10.1029/92JC00239.

McPhee, M.G., 2008. Air-Ice-Ocean Interaction, Air-Ice-Ocean Interaction: Turbulent Ocean Boundary Layer Exchange Processes. http://dx.doi.org/10.1007/978-0-387-78335-2.

McPhee, M.G., 2016. The sea ice–ocean boundary layer. In: Sea Ice. John Wiley & Sons, Ltd, Chichester, UK, pp. 138–159. http://dx.doi.org/10.1002/9781118778371.ch5.

McPhee, M.G., Kottmeier, C., Morison, J.H., 1999. Ocean heat flux in the central weddell sea during winter. J. Phys. Oceanogr. 29, 1166–1179. http://dx.doi.org/10.1175/1520-0485(1999)029<1166:OHFITC>2.0.CO;2.

McPhee, M.G., Maykut, G.A., Morison, J.H., 1987. Dynamics and thermodynamics of the ice/upper ocean system in the marginal ice zone of the Greenland sea. J. Geophys. Res. Ocean 92, 7017–7031. http://dx.doi.org/10.1029/JC092iC07p07017.

McPhee, M.G., Morison, J.H., Malyarenko, A., 2019. Ice-ocean boundary layer. Part 1: Structure. In: Encyclopedia of Ocean Sciences. Elsevier, pp. 155–165. http://dx.doi.org/10.1016/B978-0-12-409548-9.09552-X.

McPhee, M.G., Morison, J.H., Nilsen, F., 2008. Revisiting heat and salt exchange at the ice–ocean interface: Ocean flux and modeling considerations. J. Geophys. Res. 113, C06014. http://dx.doi.org/10.1029/2007JC004383.

McPhee, M.G., Proshutinsky, A., Morison, J.H., Steele, M., Alkire, M.B., 2009. Rapid change in freshwater content of the Arctic ocean. Geophys. Res. Lett. 36, L10602. http://dx.doi.org/10.1029/2009GL037525.

Meier, W.N., 2016. Losing Arctic sea ice: observations of the recent decline and the long-term context. In: Sea, Ice. John Wiley & Sons, Ltd, Chichester, UK, pp. 290–303. http://dx.doi.org/10.1002/9781118778371.ch11.

Merino, N., Jourdain, N.C., Le Sommer, J., Goosse, H., Mathiot, P., Durand, G., 2018. Impact of increasing Antarctic glacial freshwater release on regional sea-ice cover in the southern ocean. Ocean Model. 121, 76–89. http://dx.doi.org/10.1016/j.ocemod.2017.11.009.

Meyer, A., Fer, I., Sundfjord, A., Peterson, A.K., 2017. Mixing rates and vertical heat fluxes north of Svalbard from Arctic winter to spring. J. Geophys. Res. Ocean 122, 4569–4586. http://dx.doi.org/10.1002/2016JC012441.

Moffat, C., Tapia, F.J., Nittrouer, C.A., Hallet, B., Bown, F., Boldt Love, K., Iturra, C., 2018. Seasonal evolution of ocean heat supply and freshwater discharge from a rapidly retreating tidewater glacier: Jorge Montt, Patagonia. J. Geophys. Res. Ocean 123, 4200–4223. http://dx.doi.org/10.1002/2017JC013069.

Mondal, M., Gayen, B., Griffiths, R.W., Kerr, R.C., 2019. Ablation of sloping ice faces into polar seawater. J. Fluid Mech. 863, 545–571. http://dx.doi.org/10.1017/jfm.2018.970.

Monin, A.S., Yaglom, A.M., 1971. Statistical Fluid Mechanics : Mechanics of Turbulence, English ed. MIT Press, Cambridge, Mass.

Moon, T., Sutherland, D.A., Carroll, D., Felikson, D., Kehrl, L., Straneo, F., 2018. Subsurface iceberg melt key to Greenland fjord freshwater budget. Nat. Geosci. 11, 49–54. http://dx.doi.org/10.1038/s41561-017-0018-z.

Motyka, R.J., Hunter, L., Echelmeyer, K.A., Connor, C., 2003. Submarine melting at the terminus of a temperate tidewater glacier, LeConte Glacier, Alaska, USA. Ann. Glaciol. 36, 57–65. http://dx.doi.org/10.3189/172756403781816374.

Mouginot, J., Rignot, E., Scheuchl, B., 2014. Sustained increase in ice discharge from the Amundsen Sea Embayment, West Antarctica, from 1973 to 2013. Geophys. Res. Lett. 41, 1576–1584. http://dx.doi.org/10.1002/2013GL059069.

Mueller, R.D., 2014. The Effects of Thermodynamic Parameterizations, Ice Shelf Geometry, and Tides on Modeled Basal Melting of Weddell Sea Ice Shelves (Ph.D. thesis). Oregon State University.

Nakayama, Y., Menemenlis, D., Schodlok, M., Rignot, E., 2017. Amundsen and bellingshausen seas simulation with optimized ocean, sea ice, and thermodynamic ice shelf model parameters. J. Geophys. Res. Ocean. 6180–6195. http://dx.doi.org/10.1002/2016JC012538.

Naughten, K.A., Meissner, K.J., Galton-Fenzi, B.K., England, M.H., Timmermann, R., Hellmer, H.H., 2018a. Future projections of Antarctic ice shelf melting based on CMIP5 scenarios. J. Clim. 31, 5243–5261. http://dx.doi.org/10.1175/JCLI-D-17-0854.1.

Naughten, K.A., Meissner, K.J., Galton-Fenzi, B.K., England, M.H., Timmermann, R., Hellmer, H.H., Hattermann, T., Debernard, J.B., 2018b. Intercomparison of Antarctic ice-shelf, ocean, and sea-ice interactions simulated by MetROMS-iceshelf and FESOM 1.4. Geosci. Model Dev. 11, 1257–1292. http://dx.doi.org/10.5194/gmd-11-1257-2018.

Nelson, M.J.S., Queste, B.Y., Smith, I.J., Leonard, G.H., Webber, B.G.M., Hughes, K.G., 2017. Measurements of ice shelf water beneath the front of the ross ice shelf using gliders. Ann. Glaciol. 58, 41–50. http://dx.doi.org/10.1017/aog.2017.34.

Nicholls, K.W., Abrahamsen, E.P., Buck, J.J.H., Dodd, P.A., Goldblatt, C., Griffiths, G., Heywood, K.J., Hughes, N.E., Kaletzky, A., Lane-Serff, G.F., McPhail, S.D., Millard, N.W., Oliver, K.I.C., Perrett, J., Price, M.R., Pudsey, C.J., Saw, K., Stansfield, K., Stott, M.J., Wadhams, P., Webb, A.T., Wilkinson, J.P., 2006. Measurements beneath an Antarctic ice shelf using an autonomous underwater vehicle. Geophys. Res. Lett. 33, 2–5. http://dx.doi.org/10.1029/2006GL025998.

Nicholls, K.W., Makinson, K., Johnson, M.R., 1997. New oceanographic data from beneath Ronne Ice Shelf, Antarctica. Geophys. Res. Lett. 24, 167. http://dx.doi.org/10.1029/96GL03922.

Nicholls, K.W., Makinson, K., Østerhus, S., 2004. Circulation and water masses beneath the northern Ronne Ice Shelf, Antarctica. J. Geophys. Res. C Ocean. 109, 1–11. http://dx.doi.org/10.1029/2004JC002302.

Nicholls, K.W., Makinson, K., Venables, E., 2012. Ocean circulation beneath Larsen C Ice Shelf, Antarctica from in situ observations. Geophys. Res. Lett. 39, 1–6. http://dx.doi.org/10.1029/2012GL053187.

Nicholls, K.W., Østerhus, S., Makinson, K., Gammelsrød, T., Fahrbach, E., 2009. Ice-ocean processes over the continental shelf of the southern Weddell Sea, Antarctica: A review. Rev. Geophys. RG3003. http://dx.doi.org/10.1029/2007RG000250.

Nicholls, K., W, Corr, H.F.J., Stewart, C.L., Lok, L.B., Brennan, P.V., Vaughan, D.G., 2015. Instruments and methods: A ground-based radar for measuring vertical strain rates and time-varying basal melt rates in ice sheets and shelves. J. Glaciol. 61, 1079–1087. http://dx.doi.org/10.3189/2015JoG15J073.

Notz, D., 2012. Challenges in simulating sea ice in earth system models. Wiley Interdiscip. Rev. Clim. Chang 3, 509–526. http://dx.doi.org/10.1002/wcc.189.

Notz, D., Bitz, C.M., 2016. Sea ice in earth system models. Sea Ice 30, 4–325. http://dx.doi.org/10.1002/9781118778371.ch12.

Notz, D., McPhee, M.G., Worster, M.G., Maykut, G.A., Schlünzen, K.H., Eicken, H., 2003. Impact of underwater-ice evolution on Arctic summer sea ice. J. Geophys. Res. 108, 3223. http://dx.doi.org/10.1029/2001JC001173.

Ohshima, K.I., Kawamura, T., Takizawa, T., Ushio, S., 1994. Step-like structure in temperature and salinity profiles, observed near icebergs trapped by fast ice, Antarctica. J. Oceanogr. 50, 365–372. http://dx.doi.org/10.1007/BF02239522.

Owen, P.R., Thomson, W.R., 1963. Heat transfer across rough surfaces. J. Fluid Mech. 15, 321–334. http://dx.doi.org/10.1017/S0022112063000288.

Padman, L., Siegfried, M.R., Fricker, H.A., 2018. Ocean tide influences on the Antarctic and Greenland ice sheets. Rev. Geophys. 56, 142–184. http://dx.doi.org/10.1002/2016RG000546.

Pattyn, F., Favier, L., Sun, S., Durand, G., 2017. Progress in numerical modeling of Antarctic ice-sheet dynamics. Curr. Clim. Chang. Rep. 3, 174–184. http://dx.doi.org/10.1007/s40641-017-0069-7.

Payne, A.J., Holland, P.R., Shepherd, A.P., Rutt, I.C., Jenkins, A., Joughin, I., 2007. Numerical modeling of ocean-ice interactions under Pine Island Bay's ice shelf. J. Geophys. Res. Ocean 112, 1–14. http://dx.doi.org/10.1029/2006JC003733.

Pelle, T., Morlighem, M., Bondzio, J.H., 2019. Brief communication: Picop, a new ocean melt parameterization under ice shelves combining PICO and a plume model. Cryosph. 13, 1043–1049. http://dx.doi.org/10.5194/tc-13-1043-2019.

Peterson, A.K., Fer, I., McPhee, M.G., Randelhoff, A., 2017. Turbulent heat and momentum fluxes in the upper ocean under Arctic sea ice. J. Geophys. Res. Ocean 122, 1439–1456. http://dx.doi.org/10.1002/2016JC012283.

Petty, A.A., Feltham, D.L., Holland, P.R., 2013. Impact of atmospheric forcing on Antarctic continental shelf water masses. J. Phys. Oceanogr. 43, 920–940. http://dx.doi.org/10.1175/JPO-D-12-0172.1.

Pollard, D., Deconto, R.M., 2012. Description of a hybrid ice sheet-shelf model, and application to Antarctica. Geosci. Model Dev. 5, 1273–1295. http://dx.doi.org/10.5194/gmd-5-1273-2012.

Potter, J.R., Paren, J.G., 1985. Interaction between ice shelf and ocean in George VI sound, Antarctica. In: Jacobs, S.S. (Ed.), Oceanology of the Antarctic Continental Shelf. pp. 35–58. http://dx.doi.org/10.1029/AR043p0035.

Pritchard, H.D., Ligtenberg, S.R.M., Fricker, H.A., Vaughan, D.G., van den Broeke, M.R., Padman, L., 2012. Antarctic ice-sheet loss driven by basal melting of ice shelves. Nature 484, 502–505. http://dx.doi.org/10.1038/nature10968.

Purkey, S.G., Johnson, G.C., 2013. Antarctic bottom water warming and freshening: Contributions to sea level rise, ocean freshwater budgets, and global heat gain. J. Clim. 26, 6105–6122. http://dx.doi.org/10.1175/JCLI-D-12-00834.1.

Rack, F., Zook, R., Levy, R., Limeburner, R., Stewart, C.L., Williams, M.J.M., Luyendyk, B., 2012. What Lies beneath? Interdisciplinary outcomes of the ANDRILL coulman high project site surveys on the ross ice shelf. Oceanography 25, 84–89. http://dx.doi.org/10.5670/oceanog.2012.79.

Rackow, T., Wesche, C., Timmermann, R., Hellmer, H.H., Juricke, S., Jung, T., 2017. A simulation of small to giant Antarctic iceberg evolution: Differential impact on climatology estimates. J. Geophys. Res. Ocean 122, 3170–3190. http://dx.doi.org/10.1002/2016JC012513.

Ramudu, E., Hirsh, B.H., Olson, P., Gnanadesikan, A., 2016. Turbulent heat exchange between water and ice at an evolving ice–water interface. J. Fluid Mech. 798, 572–597. http://dx.doi.org/10.1017/jfm.2016.321.

Randelhoff, A., Sundfjord, A., Renner, A.H.H., 2014. Effects of a shallow pycnocline and surface meltwater on sea ice–ocean drag and turbulent heat flux. J. Phys. Oceanogr. 44, 2176–2190. http://dx.doi.org/10.1175/JPO-D-13-0231.1.

Reese, R., Albrecht, T., Mengel, M., Asay-Davis, X., Winkelmann, R., 2018. Antarctic sub-shelf melt rates via PICO. Cryosphere 12, 1969–1985. http://dx.doi.org/10.5194/tc-12-1969-2018.

Rignot, E., Jacobs, S.S., Mouginot, J., Scheuchl, B., 2013. Ice-shelf melting around Antarctica. Science 341, 266–270. http://dx.doi.org/10.1126/science.1235798.

Rignot, E., Koppes, M., Velicogna, I., 2010. Rapid submarine melting of the calving faces of west Greenland glaciers. Nat. Geosci. 3, 187–191. http://dx.doi.org/10.1038/ngeo765.

Rignot, E., Xu, Y., Menemenlis, D., Mouginot, J., Scheuchl, B., Li, X., Morlighem, M., Seroussi, H., van den Broeke, M.R., Fenty, I., Cai, C., An, L., de Fleurian, B., 2016. Modeling of ocean-induced ice melt rates of five west Greenland glaciers over the past two decades. Geophys. Res. Lett. 43, 6374–6382. http://dx.doi.org/10.1002/2016GL068784.

Robinson, N.J., Stevens, C.L., McPhee, M.G., 2017. Observations of amplified roughness from crystal accretion in the sub-ice ocean boundary layer. Geophys. Res. Lett. 1814–1822. http://dx.doi.org/10.1002/2016GL071491.

Robinson, N.J., Williams, M.J.M., Barrett, P.J., Pyne, A.R., 2010. Observations of flow and ice–ocean interaction beneath the McMurdo Ice Shelf, Antarctica. J. Geophys. Res. Ocean. 115, C03025. http://dx.doi.org/10.1029/2008JC005255.

Robinson, N.J., Williams, M.J.M., Stevens, C.L., Langhorne, P.J., Haskell, T.G., 2014. Evolution of a supercooled ice shelf water plume with an actively growing subice platelet matrix. J. Geophys. Res. Ocean 119, 3425–3446. http://dx.doi.org/10.1002/2013JC009399.

Schaffer, J., von Appen, W.-J., Dodd, P.A., Hofstede, C., Mayer, C., de Steur, L., Kanzow, T., 2017. Warm water pathways toward Nioghalvfjerdsfjorden Glacier, Northeast Greenland. Geophys. Res. Ocean. 122, 4004–4020. http://dx.doi.org/10.1002/2016JC012462.

Scheduikat, M., Olbers, D.J., 1990. A one-dimensional mixed layer model beneath the Ross Ice Shelf with tidally induced vertical mixing. Antarct. Sci. 2, http://dx.doi.org/10.1017/S0954102090000049.

Schild, K.M., Renshaw, C.E., Benn, D.I., Luckman, A., Hawley, R.L., How, P., Trusel, L., Cottier, F.R., Pramanik, A., Hulton, N.R.J., 2018. Glacier calving rates due to subglacial discharge, Fjord circulation, and free convection. J. Geophys. Res. Earth Surf. 123, 2189–2204. http://dx.doi.org/10.1029/2017JF004520.

Sciascia, R., Cenedese, C., Nicolì, D., Heimbach, P., Straneo, F., 2014. Impact of periodic intermediary flows on submarine melting of a Greenland glacier. J. Geophys. Res. Ocean 119, 7078–7098. http://dx.doi.org/10.1002/2014JC009953.

Sciascia, R., Straneo, F., Cenedese, C., Heimbach, P., 2013. Seasonal variability of submarine melt rate and circulation in an East Greenland fjord. J. Geophys. Res. Ocean 118, 2492–2506. http://dx.doi.org/10.1002/jgrc.20142.

Sergienko, O.V., Goldberg, D.N., Little, C.M., 2013. Alternative ice shelf equilibria determined by ocean environment. J. Geophys. Res. Earth Surf. 118, 970–981. http://dx.doi.org/10.1002/jgrf.20054.

Shepherd, A., Ivins, E.R., G, A., Barletta, V.R., Bentley, M.J., Bettadpur, S., Briggs, K.H., Bromwich, D.H., Forsberg, R., Galin, N., Horwath, M., Jacobs, S., Joughin, I., King, M.A., Lenaerts, J.T.M., Li, J., Ligtenberg, S.R.M., Luckman, A., Luthcke, S.B., McMillan, M., Meister, R., Milne, G., Mouginot, J., Muir, A., Nicolas, J.P., Paden, J., Payne, A.J., Pritchard, H., Rignot, E., Rott, H., Sorensen, L.S., Scambos, T.A., Scheuchl, B., Schrama, E.J.O., Smith, B., Sundal, A.V., van Angelen, J.H., van de Berg, W.J., van den Broeke, M.R., Vaughan, D.G., Velicogna, I., Wahr, J., Whitehouse, P.L., Wingham, D.J., Yi, D., Young, D., Zwally, H.J., 2012. A reconciled estimate of ice-sheet mass balance. Science 338, 1183–1189. http://dx.doi.org/10.1126/science.1228102.

Shirasawa, K., Ingram, R., 1991a. Characteristics of the turbulent oceanic boundary layer under sea ice. Part 2: Measurements in southeast Hudson Bay. J. Mar. Syst. 2, 161–169. http://dx.doi.org/10.1016/0924-7963(91)90022-M.

Shirasawa, K., Ingram, R.G., 1991b. Characteristics of the turbulent oceanic boundary layer under sea ice. Part 1: A review of the ice–ocean boundary layer. J. Mar. Syst. 2, 153–160. http://dx.doi.org/10.1016/0924-7963(91)90021-L.

Shroyer, E.L., Padman, L., Samelson, R.M., Münchow, A., Stearns, L.A., 2017. Seasonal control of petermann gletscher ice-shelf melt by the ocean's response to sea-ice cover in Nares Strait. J. Glaciol. 63, 324–330. http://dx.doi.org/10.1017/jog.2016.140.

Silva, T.A.M., Bigg, G.R., Nicholls, K.W., 2006. Contribution of giant icebergs to the Southern Ocean freshwater flux. J. Geophys. Res. Ocean 111, 1–8. http://dx.doi.org/10.1029/2004JC002843.

Silvano, A., Rintoul, S.R., Peña Molino, B., Hobbs, W.R., van Wijk, E., Aoki, S., Tamura, T., Williams, G.D., 2018. Freshening by glacial meltwater enhances melting of ice shelves and reduces formation of Antarctic bottom water. Sci. Adv. 4, eaap9467. http://dx.doi.org/10.1126/sciadv.aap9467.

Sirevaag, A., 2009. Turbulent exchange coefficients for the ice/ocean interface in case of rapid melting. Geophys. Res. Lett. 36, L04606. http://dx.doi.org/10.1029/2008GL036587.

Slater, D.A., Goldberg, D.N., Nienow, P.W., Cowton, T.R., 2016. Scalings for submarine melting at tidewater glaciers from buoyant plume theory. J. Phys. Oceanogr. 46, 1839–1855. http://dx.doi.org/10.1175/JPO-D-15-0132.1.

Slater, D.A., Nienow, P.W., Cowton, T.R., Goldberg, D.N., Sole, A.J., 2015. Effect of near-terminus subglacial hydrology on tidewater glacier submarine melt rates. Geophys. Res. Lett. 42, 2861–2868. http://dx.doi.org/10.1002/2014GL062494.

Slater, D.A., Straneo, F., Das, S.B., Richards, C.G., Wagner, T.J.W., Nienow, P.W., 2018. Localized plumes drive front-wide ocean melting of a greenlandic tidewater glacier. Geophys. Res. Lett. 45, 12, 350-12, 358. http://dx.doi.org/10.1029/2018GL080763.

Stanton, T.P., Shaw, W.J., Truffer, M., Corr, H.F.J., Peters, L.E., Riverman, K.L., Bindschadler, R., Holland, D.M., Anandakrishnan, S., 2013. Channelized ice melting in the ocean boundary layer beneath pine island glacier, antarctica. Science 341, 1236–1239. http://dx.doi.org/10.1126/science.1239373.

Steele, M., Mellor, G.L., Mcphee, M.G., 1989. Role of the molecular sublayer in the melting or freezing of sea ice. J. Phys. Oceanogr. 19, 139–147. http://dx.doi.org/10.1175/1520-0485(1989)019<0139:ROTMSI>2.0.CO;2.

Steele, M., Morison, J.H., 1993. Hydrography and vertical fluxes of heat and salt northeast of svalbard in autumn. J. Geophys. Res. 98, 10013. http://dx.doi.org/10.1029/93JC00937.

Stephenson, G.R., Sprintall, J., Gille, S.T., Vernet, M., Helly, J.J., Kaufmann, R.S., 2011. Subsurface melting of a free-floating Antarctic iceberg. Deep. Res. Part II Top. Stud. Oceanogr. 58 (11–12), 1336–1345. http://dx.doi.org/10.1016/j.dsr2.2010.11.009.

Stern, A.A., Adcroft, A., Sergienko, O., Marques, G., 2017. Modeling tabular icebergs submerged in the ocean. J. Adv. Model. Earth Syst. 9, 1948–1972. http://dx.doi.org/10.1002/2017MS001002.

Stern, A.A., Dinniman, M.S., Zagorodnov, V.S., Tyler, S.W., Holland, D.M., 2013. Intrusion of warm surface water beneath the McMurdo Ice Shelf, Antarctica. J. Geophys. Res. Ocean 118, 7036–7048. http://dx.doi.org/10.1002/2013JC008842.

Stewart, C.L., 2017. Ice-Ocean Interactions under the North-Western Ross Ice Shelf, Antarctica (Ph.D. thesis). University of Cambridge.

Stewart, C.L., Christoffersen, P., Nicholls, K.W., Williams, M.J.M., Dowdeswell, J.A., 2019. Basal melting of Ross Ice Shelf from solar heat absorption in an ice-front polynya. Nat. Geosci. 12, 435–440. http://dx.doi.org/10.1038/s41561-019-0356-0.

Straneo, F., Cenedese, C., 2015. The dynamics of greenland's glacial fjords and their role in climate. Ann. Rev. Mar. Sci. 7, 89–112. http://dx.doi.org/10.1146/annurev-marine-010213-135133.

Straneo, F., Hamilton, G.S., Sutherland, D.A., Stearns, L.A., Davidson, F., Hammill, M.O., Stenson, G.B., Rosing-Asvid, A., 2010. Rapid circulation of warm subtropical waters in a major glacial fjord in east greenland. Nat. Geosci. 3, 182–186. http://dx.doi.org/10.1038/ngeo764.

Straneo, F., Sutherland, D.A., Holland, D.M., Gladish, C., Hamilton, G.S., Johnson, H.L., Rignot, E., Xu, Y., Koppes, M., 2012. Characteristics of ocean waters reaching greenland's glaciers. Ann. Glaciol. 53, 202–210. http://dx.doi.org/10.3189/2012AoG60A059.

Sugiyama, S., Sawagaki, T., Fukuda, T., Aoki, S., 2014. Active water exchange and life near the grounding line of an Antarctic outlet glacier. Earth Planet. Sci. Lett. 399, 52–60. http://dx.doi.org/10.1016/j.epsl.2014.05.001.

Sundfjord, A., Albretsen, J., Kasajima, Y., Skogseth, R., Kohler, J., Nuth, C., Skarðhamar, J., Cottier, F., Nilsen, F., Asplin, L., Gerland, S., Torsvik, T., 2017. Effects of glacier runoff and wind on surface layer dynamics and Atlantic Water exchange in Kongsfjorden, Svalbard; a model study. Estuar. Coast. Shelf Sci. 187, 260–272. http://dx.doi.org/10.1016/j.ecss.2017.01.015.

Timmermann, R., Beckmann, A., Hellmer, H.H., 2002. Simulations of ice–ocean dynamics in the Weddell Sea 1. Model configuration and validation. J. 107, 12. http://dx.doi.org/10.1029/2000JC000741.

Timmermann, R., Hellmer, H.H., 2013. Southern ocean warming and increased ice shelf basal melting in the twenty-first and twenty-second centuries based on coupled ice–ocean finite-element modelling. Ocean Dyn. 63, 1011–1026. http://dx.doi.org/10.1007/s10236-013-0642-0.

Toppaladoddi, S., Succi, S., Wettlaufer, J.S., 2017. Roughness as a route to the ultimate regime of thermal convection. Phys. Rev. Lett. 118, 074503. http://dx.doi.org/10.1103/PhysRevLett.118.074503.

Truffer, M., Motyka, R.J., 2016. Where glaciers meet water: Subaqueous melt and its relevance to glaciers in various settings. Rev. Geophys. 54, 220–239. http://dx.doi.org/10.1002/2015RG000494.

Tsamados, M., Feltham, D., Petty, A., Schroeder, D., Flocco, D., 2015. Processes controlling surface, bottom and lateral melt of Arctic sea ice in a state of the art sea ice model. Philos. Trans. R. Soc. A Math. Phys. Eng. Sci. 373, 20140167. http://dx.doi.org/10.1098/rsta.2014.0167.

Tsamados, M., Feltham, D.L., Schroeder, D., Flocco, D., Farrell, S.L., Kurtz, N., Laxon, S.W., Bacon, S., 2014. Impact of variable atmospheric and oceanic form drag on simulations of Arctic sea ice*. J. Phys. Oceanogr. 44, 1329–1353. http://dx.doi.org/10.1175/JPO-D-13-0215.1.

Turner, J.S., 1973. Buoyancy Effects in Fluids. Cambridge University Press, Cambridge, http://dx.doi.org/10.1017/CBO9780511608827.

Turner, A.K., Hunke, E.C., 2015. Impacts of a mushy-layer thermodynamic approach in global sea-ice simulations using the CICE sea-ice model. J. Geophys. Res. Ocean 120, 1253–1275. http://dx.doi.org/10.1002/2014JC010358.

van Heijst, G.J.F., 1987. On the oceanic circulation near a shelf-ice edge. In: Van der Veen, C.J., O.J. (Eds.), Dynamics of the West Antarctic Ice Sheet. Glaciology and Quaternary Geology, vol. 4. pp. 37–56. http://dx.doi.org/10.1007/978-94-009-3745-1_3.

Vancoppenolle, M., Fichefet, T., Goosse, H., Bouillon, S., Madec, G., Maqueda, M.A.M., 2009. Simulating the mass balance and salinity of Arctic and Antarctic sea ice. 1. Model description and validation. Ocean Model. 27, 33–53. http://dx.doi.org/10.1016/j.ocemod.2008.10.005.

Vreugdenhil, C.A., Taylor, J.R., 2019. Stratification effects in the turbulent boundary layer beneath a melting ice shelf: insights from resolved large-eddy simulations. J. Phys. Oceanogr. 49 (7), 1905–1925.

Wåhlin, J., Klein-Paste, A., 2017. The effect of mass diffusion on the rate of chemical ice melting using aqueous solutions. Cold Reg. Sci. Technol. 139, 11–21. http://dx.doi.org/10.1016/j.coldregions.2017.04.001.

Weingartner, T.J., Danielson, S.L., Potter, R.A., Trefry, J.H., Mahoney, A., Savoie, M., Irvine, C., Sousa, L., 2017. Circulation and water properties in the landfast ice zone of the Alaskan Beaufort Sea. Cont. Shelf Res. 148, 185–198. http://dx.doi.org/10.1016/j.csr.2017.09.001.

Wells, A.J., 2008. Natural Convection Boundary Layers and their Influence on Phase Change in the Polar Oceans (Ph.D. thesis). University of Cambridge.

Wells, A.J., Worster, M.G., 2008. A geophysical-scale model of vertical natural convection boundary layers. J. Fluid Mech. 609, 111–137. http://dx.doi.org/10.1017/S0022112008002346.

Wells, A.J., Worster, M.G., 2011. Melting and dissolving of a vertical solid surface with laminar compositional convection. J. Fluid Mech. 687, 118–140. http://dx.doi.org/10.1017/jfm.2011.322.

Wilchinsky, A.V., Feltham, D.L., Holland, P.R., 2007. The effect of a new drag-law parameterization on ice shelf water plume dynamics. J. Phys. Oceanogr. 37, 1778–1792. http://dx.doi.org/10.1175/JPO3093.1.

Woods, A.W., 1992. Melting and dissolving. J. Fluid Mech. 239, 429. http://dx.doi.org/10.1017/S0022112092004476.

Xu, Y., Rignot, E., Fenty, I., Menemenlis, D., Flexas, M.M., 2013. Subaqueous melting of store glacier, west Greenland from three-dimensional, high-resolution numerical modeling and ocean observations. Geophys. Res. Lett. 40, 4648–4653. http://dx.doi.org/10.1002/grl.50825.

Xu, Y., Rignot, E., Menemenlis, D., Koppes, M., 2012. Numerical experiments on subaqueous melting of Greenland tidewater glaciers in response to ocean warming and enhanced subglacial discharge. Ann. Glaciol. 53, 229–234. http://dx.doi.org/10.3189/2012AoG60A139.

Yaglom, A.M., Kader, B.A., 1974. Heat and mass transfer between a rough wall and turbulent fluid flow at high Reynolds and Peclet numbers. J. Fluid Mech. 62, 601–623.

Yankovsky, A.E., Yashayaev, I., 2014. Surface buoyant plumes from melting icebergs in the Labrador Sea. Deep. Res. Part I Oceanogr. Res. Pap. 91, 1–9. http://dx.doi.org/10.1016/j.dsr.2014.05.014.

Zhu, X., Stevens, R.J.A.M., Verzicco, R., Lohse, D., 2017. Roughness-facilitated local 1/2 scaling does not imply the onset of the ultimate regime of thermal convection. Phys. Rev. Lett. 119, 154501. http://dx.doi.org/10.1103/PhysRevLett.119.154501.